Fibronectin Extra Domains tune cellular responses and confer topographically distinct features to fibril networks

Georgios Efthymiou, Agata Radwanska, Anca-Ioana Grapa, Stéphanie Beghelli-de La Forest Divonne, Dominique Grall, Sébastien Schaub, Maurice Hattab, Sabrina Pisano, M. Poët, Didier F Pisani, et al.

Fibronectin Extra Domains tune cellular responses and confer topographically distinct features to fibril networks

Georgios Efthymiou[1]‡, Agata Radwanska[1]‡, Anca-Ioana Grapa[1,2], Stéphanie Beghelli-de la Forest Divonne[1,3], Dominique Grall[1], Sébastien Schaub[1], Maurice Hattab[1], Sabrina Pisano[4], Mallorie Poet[4], Didier F. Pisani[5], Laurent Counillon[5], Xavier Descombes[2], Laure Blanc-Féraud[2], and Ellen Van Obberghen-Schilling[1]*

[1]Université Côte d'Azur, CNRS, INSERM, iBV, Nice, France

[2]Université Côte d'Azur, Inria, CNRS, i3S, Nice, France

[3]Centre Antoine Lacassagne, Nice, France

[4]Université Côte d'Azur, Inserm, CNRS, IRCAN, Nice, France

[5]Université Côte d'Azur, CNRS, LP2M, Nice, France

‡ These authors contributed equally to this work

* Corresponding author:

Ellen Van Obberghen-Schilling

Institut de Biologie Valrose (iBV)

CNRS – INSERM – UCA

Université Côte d'Azur

Parc Valrose

06108 Nice cedex 2, FRANCE

Tel +33 (0)4 89 15 0790

E-mail: vanobber@unice.fr

Running title: Alternatively spliced fibronectin variants

Word count: 7166 Words

Keywords: Fibronectin, Extracellular matrix, Oncofetal isoforms, Alternative splicing, Fibronectin fibrillogenesis, Fibroblasts

Summary statement

Fibronectin, a major building block of tissues and organs, tunes fibroblast behavior and matrix architecture through the presence of alternatively spliced extra domains.

Abstract

Cellular fibronectin (FN; also known as FN1) variants harboring one or two alternatively spliced so-called extra domains (EDB and EDA) play a central bioregulatory role during development, repair processes and fibrosis. Yet, how the extra domains impact fibrillar assembly and function of the molecule remains unclear. Leveraging a unique biological toolset and image analysis pipeline for direct comparison of the variants, we demonstrate that the presence of one or both extra domains impacts FN assembly, function and physical properties of the matrix. When presented to FN-null fibroblasts, extra domain-containing variants differentially regulate pH homeostasis, survival, and TGF-β signaling by tuning the magnitude of cellular responses, rather than triggering independent molecular switches. Numerical analyses of fiber topologies highlight significant differences in variant-specific structural features and provide a first step for the development of a generative model of FN networks to unravel assembly mechanisms and investigate the physical and functional versatility of extracellular matrix landscapes.

Introduction

The extracellular matrix (ECM) is a cell-derived bioscaffold composed of more than 100 proteins in a given tissue (Hynes and Naba, 2012) that provides mechanical support to the underlying cells and promotes tissue integrity. In addition, the composition and the physical state of the ECM affect cell physiology by acting as a functionalized platform for the transmission of biochemical and biomechanical cues [reviewed in (Frantz et al., 2010; Hynes, 2009; Theocharis et al., 2016)]. Fibronectin (FN; also known as FN1), a major ECM component of developing and diseased tissues, is at the epicenter of this platform.

FN is a large glycoprotein composed of two similar, but not identical, subunits, encoded by a single gene and linked by two disulfide bonds at their C-terminal ends. Each subunit (240-270 kDa) has a repetitive modular structure composed of Type I, Type II, and highly extensible Type III repeats that allow the molecule to acquire compact and stretched conformations and to partner with a large variety of ECM components, cell receptors and soluble factors in a mechanically-tuned fashion (Vogel, 2006). FN is assembled into a fibrillar array, its active form, on the surface of assembly-competent cells. Fibrillogenesis

is initiated by the binding of FN to its principal cellular receptor, integrin $\alpha5\beta1$. Integrin activation triggers the recruitment of cytoplasmic binding partners and reorganization of the actin cytoskeleton. Intracellular acto-myosin-generated forces applied to FN lead to partial unfolding of the molecule and exposure of cryptic self-association sites that support polymerization and higher-order fiber assembly on the cell surface, as reviewed in (Singh et al., 2010). Importantly, FN networks provide templates for the deposition of other matrix proteins (Sottile and Hocking, 2002; Velling et al., 2002).

FN can be found in two distinct forms known as plasma FN (pFN) and cellular FN (cFN). pFN is produced by the liver and circulates in the bloodstream, while cellular FN (cFN) is expressed and assembled in an insoluble matrix by mesenchymal cells such as fibroblasts, endothelial cells, chondrocytes and macrophages (Hynes, 1990). cFN differs from pFN by the presence of highly conserved [reviewed in (White et al., 2008)] alternatively spliced FN Type III repeats termed extra domain B (EDB or EIIIB) and extra domain A (EDA or EIIIA), which flank the cell binding (RGD) and synergy sites (PHSRN) located in FNIII10 and FNIII9, respectively. Each alternatively spliced extra domain is generated from a single exon and gives rise to a FNIII repeat, the expression of which is tightly regulated and limited to embryonic development, wound healing (Ffrench-Constant, 1989), and tumor progression (Castellani, 1986). Thus, the term "oncofetal" is often used to describe FN isoforms harboring either or both of the extra domains, that are scarce in adult tissues.

Early knockout studies in the mouse highlighted the importance of FN in the developing organism, since FN-null mice die during gestation [before embryonic day (E)10.5] due to severe defects in neural tube formation and vascular development (George et al., 1993). Intriguingly, combined deletion of both extra domains also leads to embryonic lethality (Astrof et al., 2007), whereas mice lacking either extra domain are viable and fertile (Fukuda et al., 2002; Muro et al., 2003). EDA-targeted deletion and EDA-constitutive inclusion studies have revealed roles for this FNIII repeat in lymphatic valve morphogenesis, atherosclerosis, tissue injury, inflammation, and lifespan regulation. While several receptors have been shown to bind EDA, such as integrins $\alpha9\beta1$, $\alpha4\beta1$, $\alpha7\beta1$, and TLR4 [reviewed in (White et al., 2008)], much less is known about EDB, for which no receptor has so far been identified. Rather, its presence has been demonstrated to induce conformational changes regulating the accessibility to adjacent cryptic sites (Balza et al., 2009; Carnemolla et al., 1992; Ventura et al., 2010), and facilitating RGD presentation to $\alpha5\beta1$ integrins, thereby favoring integrin clustering and downstream signaling (Schiefner et al., 2012).

Regarding matrix assembly, FNs containing EDB or EDA have been found to be most efficiently integrated by cells into pre-existing ECMs (Guan et al., 1990), consistent with subsequent loss-of-function studies

showing that EDB deficiency reduced FN deposition in cultured fibroblasts and endothelial cells (Cseh et al., 2010; Fukuda et al., 2002). These data suggest, that although the extra domains are not essential for FN fibrillogenesis per se, they may regulate the dynamics of polymerization by affecting FN-cell and/or FN-FN interactions.

Despite decades of research on fibronectin, the role of extra domains in FN assembly and functions has not been directly assessed using full-length variants in an identical cellular context, devoid of autocrine FN production. To this end, we generated constructs harboring human FN variants containing one, both, or none of the alternatively spliced extra domains for expression in FN-null cells, and production of recombinant proteins in assembly-incompetent cells. As the biological activity of FN is dependent on the conformation of the fibers that constitute its functional form, we enriched our biological toolset with in-depth computational analyses of FN network topology. Here, we report that the presence of EDB and/or EDA facilitates FN fibrillogenesis and regulates cell survival, pH control, and TGF-β signaling in fibroblasts. Quantitative characterization of FN networks has uncovered significant variant-specific differences in structural features and provides a promising framework to enrich the development of imaging-based machine learning methodologies for automatic classification of matrix attributes associated with disease states.

Results

Recombinant human FN isoforms

To explore the functions of alternatively spliced cFN variants and the impact of the extra domains EDB and EDA on FN matrix assembly, we constructed a set of lentiviral expression vectors harboring the full-length coding sequence of the human *FN1* gene containing one, both or none of these alternatively spliced FN Type III repeats (**Fig. 1A**). All constructs contain the alternatively spliced variable region V-89 (Schwarzbauer, 1991). We chose not to insert additional sequences encoding cumbersome fluorescent proteins or molecular tags, to avoid modifying the conformation of the protein and disrupting inter- and intra-molecular interactions.

Re-expression of FN variants in FN-null MFs

To eliminate confounding effects of endogenous cFN for re-expression studies, a Cre recombinase vector was introduced in *Fn1 fl/fl* mouse fibroblasts (MFs), which express FN EDB- and EDA-containing transcripts at a ratio of roughly 1:1 (**Fig. S1A-C**). One *Fn1 -/-* clone (clone D) was selected for transduction with the

human FN expression vectors based on its fibroblast morphology, its ability to readily assemble exogenously presented FN and the absence of multinucleated and/or senescent cells (**Fig. S1D,E**). Following transduction, variant-expressing clones were isolated for analysis, as working with homogeneous populations of FN-re-expressing cells, rather than heterogeneous populations with highly variable FN expression levels, is essential for comparative studies (**Fig. 1A**). Furthermore, for comparison, equivalent amounts of FN must be expressed by the selected clones.

A representative clone of each variant is shown in **Fig. 1B-D**. The presence of the expected extra domains in the pericellular FN matrix was confirmed by immunofluorescence staining with extra domain-specific antibodies (**Fig. S2A**). Despite relatively similar FN transcript levels (**Fig. 1B**), more cell-associated FN was observed in lysates of MF clones expressing the extra domain-containing variants than the plasma-like FN B-A-. Conversely, the ratio of soluble FN in the conditioned medium to cell-associated FN was higher in MFs expressing plasma-like FN B-A- (**Fig. 1C**). The facilitating effect of the extra domains on FN assembly was further evidenced by the augmented pericellular deposition of fibers by clones expressing extra domain-containing FN (**Fig. 1D**).

We have previously demonstrated that autocrine FN expression is tightly coupled to its fibrillar assembly and that differences in FN expression levels could have a considerable effect on assembly of the protein (Cseh et al., 2010). Indeed, examination of several variant-expressing clones (**Fig. S2B-D**) confirmed that increased expression of the same mRNA generally resulted in more efficient assembly of the molecule. Nonetheless, some clones expressing equivalent amounts of the same transcript displayed marked differences in their ability to deposit a FN matrix, indicating that not only expression levels, but clonal heterogeneity can also impact fibrillogenesis.

These re-expression studies indicate that cells assemble FN containing either one or both of the extra domains more efficiently than FN lacking extra domains. However, our findings that FN assembly is particularly sensitive to autocrine expression levels and to clonal variability indicate that direct comparison of FN variant assembly and function cannot be accurately achieved using clones that re-express FN.

Presentation of recombinant variants to FN-deficient MFs

To circumvent the problems associated with the inherent phenotypic variability of recipient MF clones, subsequent studies were performed in an identical cellular context. Hence, as schematized in **Fig. 2A**, FN

147 variants were purified and provided in soluble form to the same *Fn1 -/-* MF clone (clone D) that was used
148 for FN re-expression studies.

149 For purification, the recombinant isoforms were expressed in assembly-incompetent HEK293 cells in
150 which endogenous FN expression is very low (**Fig. S3A,B**). Following transduction, cells secreted high levels
151 of the soluble variants into their culture medium. The purified variants displayed appropriate molecular
152 mass and they dimerized (**Fig. S3C**), as required for fibrillogenesis (Schwarzbauer, 1991). Specific inclusion
153 of each extra domain was confirmed by western blot analysis using isoform-specific anti-FN antibodies
154 (**Fig. S3D**). Cellular FN is considerably less soluble than pFN under physiological buffer conditions (Yamada
155 and Olden 1978). Consequently, it was essential to assure concentration uniformity of the soluble proteins
156 in each experiment and verify the absence of FN aggregates, visualized by immunofluorescence staining
157 of FN variant-coated coverslips (**Fig. S3E** arrowheads).

158 For analysis of FN assembly, subconfluent *Fn1 -/-* MFs were allowed to adhere overnight on non-coated
159 glass coverslips before adding the variants. A concentration of 15 µg/ml was chosen for experiments,
160 following dose-response analyses of exogenous FN assembly by these cells (**Fig. S3F**). First, we compared
161 the quantity of the different recombinant FNs in cell lysates by western blotting. As shown in **Fig. 2B**, all
162 of the FN variants were readily detectable as early as 2 h after addition of the soluble proteins to the cells.
163 Variants containing one or both extra domains were 1.69- to 3.18-fold more abundant in cell lysates than
164 plasma-like FN. The cell-associated protein corresponded exclusively to assembled FN, as determined by
165 immunofluorescence staining (**Fig. 2C**).

166 Similar to what was observed in FN re-expressing cells (**Fig. 1D**), the presence of extra domains enhanced
167 fibrillar assembly of exogenous FN (**Fig. 2C**). Whereas only short thin fibers were detected at 2 h on cells
168 presented with plasma-like FN, a more elaborate pattern of long, coarse fibers was seen in cells treated
169 with the cFN variants. At 2 h we did not observe marked variant-specific patterns of cFN assembly (**Fig.**
170 **2C)**, or extra domain-dependent differences in integrin distribution (**Fig. S4**). Assembly of the exogenously
171 provided cFN was predominantly observed at sites of cell-cell adhesion (**Fig. 2C,** thick arrow), or along the
172 lateral and retracting edges of polarized cells (**Fig. 2C,** thin arrow). FN fibrils were not present in the
173 peripheral adhesions at the front of polarized cells (**Fig. 2C,** arrowhead). By 48 h all four recombinant FN
174 variants were incorporated into dense meshworks by cells (**Fig. 2C**).

175 **Effect of FN variants on cell growth and survival**

The presence of EDB and EDA in cellular FN have been reported to confer distinct growth promoting properties upon the molecule (Fukuda et al., 2002; Manabe et al., 1999). Therefore, we examined the proliferative effects of the recombinant full-length cFN variants on *Fn1 -/-* MFs. As shown in **Fig. 3A**, addition of FN had no significant effect on early growth of cells. All four FN variants significantly increased exponential growth rates (decreased cell doubling times) compared to that of vehicle-treated control (CTRL) cells (**Fig. 3B**). Interestingly, whereas the number of viable cells began to plateau after 3 days in vehicle-treated cultures and after 4 days in presence of plasma-like FN B-A-, the numbers of cells in cultures with FN containing one or both extra domains continued to increase for at least 5 days. At 5 days, CTRL- and FN B-A- -treated cultures displayed an increased number of round, refractory (dying) cells, compared to cells treated with extra domain-containing FN variants, as depicted in the phase contrast images of FN B-A- and FN B+A+-treated monolayers (**Fig. 3C**). This finding suggests that the cFN variants confer a survival advantage to densely packed cells.

Metabolic effects of FN

While performing growth curve experiments, we observed an increase in acidification of the culture medium of cells treated with the extra domain-containing FN variants, as compared to CTRL (non-treated) cells or cells exposed to plasma-like FN B-A- (**Fig. 3D**). The effect became visible after 2 days and the increment was most pronounced in cells presented with FN B+A-, despite the similar growth rate of these cells (**Fig. 3A,B**). Extracellular acidification is a proxy for lactate production suggesting that FN-induced acidification of the intra- and extra-cellular space could be due to a metabolic switch in the cells from oxidative phosphorylation to anaerobic glycolysis. To assess this, we measured glucose uptake, lactate production, the extracellular acidification rate (ECAR) and the oxygen consumption rate (OCR) in CTRL and FN variant-treated cells.

Glucose transport and lactate extrusion measurements after 48 h showed a tendency for FN-induced stimulation, although statistical significance was not reached (**Fig. S5A,B**). Moreover, expression of glycolytic enzymes was significantly increased by FN (**Fig. S5C,D**), yet no variant-dependent differences were detected. Next, we determined glycolysis and mitochondrial respiration simultaneously after 72 h of FN treatment. Compared to CTRL cells, FN B+A- and FN B-A+ -treated cells displayed a higher basal extracellular acidification rate (ECAR) (**Fig. 3E**), and this is in line with medium color changes. ECAR in response to glucose addition, reflecting anaerobic glycolytic response, remained unchanged across conditions, and even slightly decreased in cells treated with FN B-A+ and B+A+ (**Fig. S5E**). Cells in presence of FN B+A+ displayed lower mitochondrial activity (lower basal OCR and lower maximal OCR) although no

differences in OCR were observed in cells treated with the other variants (**Fig. S5F,G**). Respiration coupled to ATP synthase was similar for all conditions and mitochondrial capacity was maximal, even without glucose, as evidenced by the same values in basal and maximal OCR, suggesting the use of another substrate for oxidative phosphorylation in these cells (**Fig. 3F** and **Fig. S5H,I**). As H^+ extrusion can be a consequence of cell acidification, we set out to detect changes in intracellular pH in cells treated with the FN variants (**Fig. 3G**). Indeed, when intracellular pH drops, several pumps extrude H^+ to bring the pH back to normal levels. While intracellular pH decreased significantly in the presence of FN B+A-, only a tendency towards a decrease was observed for B-A+ -treated cells (**Fig. 3G**) which displayed increased ECAR (**Fig. 3E**). From these results, we conclude that addition of exogenous FN to these fibroblasts does not induce a readily apparent metabolic reprogramming but does induce H^+ extrusion partly independent of anaerobic glycolysis, and this effect is influenced by the presence of extra domains.

FN-induced TGF-β activation and signaling

It has been previously proposed that ECM formation and turnover depend on a feed forward loop involving FN and TGF-β (Fontana et al., 2005). TGF-β regulates FN production (Ignotz and Massagué, 1986), alternative splicing (Balza et al., 1988; Borsi et al., 1990; Castellani, 1986), and the expression of the major FN receptor, integrin α5β1 (Ignotz and Massagué, 1987). Moreover, FN was shown to mediate latent TGF-β activation through a mechanism involving αv-containing integrins (Fontana et al. 2005; Henderson et al. 2013). To assess whether the extra domains play a role in FN-induced activation of latent TGF-β and TGF-β signaling in *Fn1 -/-* MFs, we monitored expression of the TGF-β response genes *PAI1* (also known as *SERPINE1*), *CTGF* (*CCN2*) and *TGFBI* (Kutz et al., 2001; Leask and Abraham, 2003; Ween et al., 2012), and SMAD2 phosphorylation (**Fig. 4**). The absence of TGF-β in our FN preparations was confirmed by ELISA (**Fig. S5J**). Time courses of *PAI1*, *CTGF* and *TGFBI* mRNA expression following the addition of 15 µg/ml of FN to cells are shown in **Fig. 4A**. FN stimulated a rapid increase in PAI1 and CTGF mRNA expression which peaked at 2 h and returned to near-basal levels by 6 h, indicating that FN triggers TGF-β signaling in *Fn1 -/-* MFs. TGFBI (TGF-β-induced) mRNA expression was unaffected at short times after FN addition (2 h). However, significant downregulation was observed after 48 h (**Fig. 4B**), reflecting a possible FN-dependent retro-control of TGF-β pathway activation. Consistent with this being a TGF-β-mediated effect on gene expression, FN also stimulated SMAD2 phosphorylation in these cells, and the presence of one or both FN extra domains had a similar impact on the magnitude of the response (**Fig. 4C**). FN B+A+ was found to be the most potent agonist of TGF-β signaling in MFs (**Fig. 4A-C**) whereas FN B-A+ induced the weakest response. The observed differences were not due to differential expression

and/or secretion of TGF-β, since total TGF-β levels in acid-treated conditioned medium were equivalent across conditions (**Fig. S5K**). As shown in **Fig. 4D**, a 30-minute pretreatment of cells with the TGFβRI antagonist SB-431542 (10μM) precluded FN-induced SMAD2 phosphorylation, indicating that this effect is mediated by TGFβRI. These results suggest that the extent of TGF-β induction most likely involves variant-specific activation of latent TGF-β. In light of the proposed role of mechanical force and ECM stiffness in activation of latent TGF-β (Hinz, 2015; Sarrazy et al., 2014; Wipff et al., 2007), we compared the ability of the FN variants to induce collagen lattice contraction by embedding *Fn1 -/-* MFs into collagen lattices containing 15 μg/ml of the FN variants. The extent of contraction was determined after 24 h. Whereas the presence of FN resulted in pronounced reduction in the lattice surface, only slight differences were observed among the four variants, indicating that presence of the extra domains had no impact on FN-induced collagen gel contraction (**Fig. S5L**).

The effect of the FN extra domains on physical properties of the ECM

As the presence of the extra domains enhanced FN fibrillogenesis and differentially affected cellular responses to FN, we examined whether variant-specific differences could be observed in the physical properties of the matrix assembled by FN-deficient MFs presented with the purified FN proteins. For optimal comparison of the matrix networks, MF cultures plated at 80% confluence were denuded of cells after 7 days and MF-derived matrices (MDMs) were fixed and stained for FN, or other matrix proteins. Interestingly, the organization of FN in the MDMs appeared to be different, depending upon the FN variant presented to cells (**Fig. 5A**). In line with its role as an obligate template for assembly of other matrix components, the architecture of FN fibrils impacted higher order matrix organization. For example, patterns of collagen VI and tenascin C staining appeared similar in mature matrices of cells presented with the same FN variant, whereas they appeared clearly dissimilar in matrices of cells presented with different variants. Differences in the mechanical properties of the four matrices were also noted. The average thickness of the MDMs ranged between 6.3 μm and 9.0 μm, with the matrix containing FN B+A- being significantly thicker than the others (**Fig. 5B**). Interestingly, the same matrix was also the most compliant, as determined by indentation using atomic force microscopy (AFM) (**Fig. 5C**). By contrast, the median Young's (elastic) modulus was highest for the MDM containing plasma-like FN, devoid of extra domains, suggesting that their presence in FN can alter the stiffness of the FN-rich ECM. Additionally, the elastic modulus of the FN B-A- MDM displayed the largest range of values suggesting a greater heterogeneity in the composition and/or crosslinking of this matrix.

Structural features of the FN variant matrices

Structural features of the ECM reflect the physiological state of tissues and have a profound impact on cell behavior. To delve deeper into the impact of FN extra domains on fiber network architecture, we employed a computational image analysis approach. Advanced computer vision and machine learning tools were developed to interrogate whether the geometric features of the variant-specific matrices (assembled by the same cells) are distinguishable, and if so, whether they can be described, quantified, modelled, or attributed to extra domain-specific biological functions.

Automatic classification of images of extra-domain-specific FN networks

To optimize the quality of the images for processing, high-resolution images of the decellularized matrices were acquired by confocal microscopy (**Fig. 6A**). Images were subsequently classified using a pre-trained convolutional neural network (CNN), as described in Materials and Methods. The results of this classification are presented in **Fig. 6B** in terms of a confusion matrix, which allows the visualization (on the diagonal) of the percentage of images that were correctly classified as belonging to the expected FN variant class. High intra-variant accuracy scores were observed (general accuracy, 83.3%), indicating that the information contained in the images is sufficient for the algorithm to recognize topological and geometrical differences inherent to the four matrix types. Additionally, machine-based classification outperformed the ability of a biologist who was blind to the experimental conditions to correctly classify the same image set (biologist accuracy, 61.4%). Topological and geometrical properties of fiber arrangements containing only EDA (B-A+) are the most distinguishable (90.5%), followed by the B-A- fibers (85.7%), devoid of extra domains. FN networks containing only EDB (B+A-) are less distinguishable, while B+A+ fibers are the least distinguishable in automatic classification.

Network properties and feature extraction

As a first step in the characterization of the properties of FN fiber networks, fibrillar structures were detected using the workflow shown in **Fig. 6C**. After generating a high-quality dataset of images (1), we defined a set of Gabor kernels, or "dictionary of elementary fibers" (2) that incorporates a set of parameters (described in Materials and methods) that capture the entire range of different fibers. After fiber detection (3), the morphological skeleton, or median axis, of the detected fibers was computed (4) for feature extraction and analysis (5). **Fig. 6D** displays the FN variant-specific graphs, or sets of edges connected by nodes, associated to the morphological skeletons of the fibers. The advantage of using a graph-based representation is that apart from Gabor-specific descriptive parameters, we are able to compute additional features that, in turn, can help characterize the properties of the FN fibers including network connectivity and mesh shape.

PCA analysis of the fiber features

After establishing a faithful representation of the fibers, a set of features was selected to characterize fiber networks and to perform principal component analysis (PCA). The PCA method was used to explore the relatedness between the different FN variants with respect to various physical attributes, or features, including i) connectivity, ii) fiber thickness, iii) fiber heterogeneity, iv) pore shape and v) pore size distribution. To describe the connectivity of the fibers, we computed the relative abundance of nodes of different degrees. The degree of every node is defined by the number of edges connected to it. The variant-specific connectivity distributions are shown in **Fig. S6A**. Interestingly, B-A- fibers are characterized by a higher abundance of fiber ends, delineating a low level of connectivity, compared to the other variants, especially to B-A+. These results reveal that the absence of extra domains leads to a less branched FN fiber arrangement.

Next, we considered fiber thickness by computing the proportion of thin to thick fibers. As shown in **Fig. S6B**, B-A- fibers display low proportion of thin fibers, and, hence, are characterized by the presence of medium and thick fibers, while the opposite is observed for B-A+. To analyze fiber thickness heterogeneity, or fiber diversity, we implemented the fiber thickness kurtosis, a parameter that indicates how outlier-prone the fiber thickness distribution is relative to a normal distribution with identical variance. In terms of fiber thickness, B-A+ values are distributed around the mean, suggesting a high homogeneity in fiber thickness, compared to B-A- fibers, the thickness of which is more heterogeneous (**Fig. S6C**).

Pore shape was measured through a circularity parameter and the average pore size. Circularity reflects pore anisotropy allowing us to distinguish circular and oval-like pores. **Fig. S6D** shows that FN B-A- arrangements are characterized by a high number of oval pores, while pores in FN B-A+ networks are predominantly circular. The same pattern is observed in terms of pore size. Large pore sizes are found within FN B-A- networks, while smaller pore size is observed in FN B-A+ networks (**Fig. S6E**).

The PCA (**Fig. 6E**) was performed with the aforementioned features, by adopting the representation provided by the first two principal components. The plot illustrates both the samples (images) projected in a bi-dimensional space, and the five features represented by vectors, the direction and length of which indicate the contribution of each feature to the two principal components. Generally, the samples belonging to FN B-A- and FN B-A+ are concentrated in non-overlapping areas, displaying the distinguishability of these two variant-specific FN networks through the chosen features.

Altogether, these analyses demonstrate that FN B-A+ matrices display highly branched, homogeneous, thin fibers that form small pores. In contrast, cells presented with FN B-A- assemble thicker, less branched fibrillar networks with larger more elongated pores. Interestingly, the presence of EDB results in matrices (either B+A-, or B+A+) characterized by a mixture of the attributes seen in B-A- and B-A+ networks.

Discussion

In this study we set out to determine how the presence of EDB and EDA in the FN molecule influences cellular functions and impacts ECM architecture. To do so we implemented an in vitro approach consisting of FN-null MFs either re-expressing or presented with extra-domain-specific FN. Several important considerations were factored into the design of our experiments: First, we used FN knock-out cells to preclude interference from endogenous cFN. Second, we generated full-length FN constructs (instead of FN fragments) in light of the involvement of multiple domains in matrix assembly [(Ohashi and Erickson, 2011) and references therein]. Furthermore, we did not include additional sequences in our constructs [e.g. GFP or YFP (Ohashi et al., 1999; Ohashi et al., 2002)] to preserve variant-specific spatial conformations and avoid disrupting relevant intra-/inter-molecular interactions, thus improving the biological relevance of our results. Finally, we learned from close examination of multiple clones re-expressing FN variants that defining the precise mechanisms by which EDB and EDA selectively impact fiber assembly and network topology is not possible in a re-expression context. Indeed, assembly of the same variant by different clones was extremely sensitive to FN expression levels and to clonal variability. This is not surprising as FN expression in vivo is exquisitely regulated, both positively and negatively and at multiple levels (transcription and mRNA processing, trafficking, secretion and assembly). Such dynamic regulation is lost upon re-expression of cDNA sequences under an exogenous promoter and lacking untranslated regions of the mRNA. Thus, dose-dependence and cell heterogeneity must be considered when investigating FN assembly in genetically-engineered cell clones or in cells with different genetic backgrounds, such as MFs isolated from different mice [e.g. control and knockout genotypes (Bass et al., 2007; Fukuda et al., 2002; Goetz et al., 2011)]. Although our variant re-expressing clones are of limited use for comparative mechanistic studies, they will be valuable resources for analyzing extra domain-specific paracrine effects of cFN-rich matrices. In addition, the availability of the expression vectors and recombinant variants described here provides not only a means of interrogating specific variant functions, but also a stepping stone for the production and investigation of matrices containing different ratios of FN variants and thus mimicking the heterogeneous FN networks observed in vivo.

A key point of our study is the enhanced fibrillar assembly of FN that contains either one or both extra domains by fibroblasts. This finding is highly relevant as cFN is a key provisional matrix component and fibroblasts are the major provisional matrix-producing cells in both physiological and pathological states such as during wound healing, inflammation, fibrosis [reviewed in (Yusuf et al., 2013)], and cancer [reviewed in (Alkasalias et al., 2018)]. Our data are consistent with data from a previous study demonstrating that recombinant rat FNs containing EDB, or EDB together with EDA, were three times more readily incorporated in pre-existing matrices of NIH 3T3 cells than FN lacking extra domains (Guan et al., 1990). More recently, antibody-based approaches (Ventura et al., 2016) and structural analysis of recombinant FN fragments (Schiefner et al., 2012) have shed light on EDB-dependent conformational changes in FN that could impact macromolecular fibril formation. In view of their crystallographic study (Schiefner et al., 2012) and other published data [reviewed in (Mezzenga and Mitsi, 2019)], Schiefner and colleagues proposed that conformational changes resulting from insertion of EDB stabilize head-to-tail homo-dimerization of FN molecules leading to the formation of a quaternary structure that enhances $\alpha5\beta1$ integrin clustering and downstream signaling. Our data would support such a mechanism and suggest that in addition to EDB, the presence of EDA may enhance FN fibrillogenesis through conformational changes that affect self-association of the molecule and how it interacts with the cellular receptors. Indeed, FN conformation affects its interactions with not only receptors, but also with proteoglycan co-receptors in the ECM and at the cell surface, which can, in turn, impact FN assembly. Conformational differences in the FN variants that affect their intermolecular interactions with other matrix proteins (collagens, tenascin C, periostin, etc.) or matrix-associated proteins (LoxL2, transglutaminase or BMP-1) could also impact the growth of FN fibrils on cell surfaces and the higher order assembly of the ECM. Finally, extra domain-specific effects on intramolecular interactions that affect the solubility of the protein are likely to affect its deposition (Castelletti et al., 2008).

Our findings that FN variants harboring the extra domains induced a decrease in intra- and extra-cellular pH in *Fn1 -/-* MFs and sustained cell growth in dense conditions, as compared to plasma-like FN, was intriguing. The generation of an acidic environment is a common feature of rapidly proliferating cells during several physiological processes (wound healing) and in fibrotic states. Extracellular acidification, best studied in tumor tissue, occurs through the reprogramming of energy metabolism in tumor cells. Moreover, increased glycolysis in the cancer-associated stroma has been proposed to provide high energy metabolites to neighboring cancer cells via what was termed the reverse Warburg effect (Pavlides et al., 2009; Yoshida, 2015). As fibroblasts are the major matrix-producing cells of epithelial tumors, and cellular FN is a major matrix constituent of the carcinoma-associated fibroblast matrisome (Gopal et al., 2017), it

was tempting to speculate that FN could actively contribute to acidification of the tumor microenvironment by stimulating Warburg-like glycolytic rates in stromal cells. Although FN-treatment of MFs led to increased mRNA expression of glycolytic enzymes and a tendency for increased glucose uptake and lactate extrusion, we failed to detect significant increases in anaerobic glycolysis (ECAR) or downregulation of mitochondrial respiration (OCR) in MFs under standard culture conditions. It will be interesting to investigate the role of cFN-regulated metabolic reprogramming of stromal fibroblasts in the tumor setting.

It is well documented that cFN expression and ECM deposition are intimately linked to TGF-β signaling in fibroblasts. In an in vivo context, FN containing the EDA domain has been identified as an important protagonist in the TGF-β-mediated conversion of precursor cells into myofibroblasts in several fibrotic disorders (Arslan et al., 2011; Booth et al., 2012; Hirshoren et al., 2013; Kohan et al., 2011; Muro et al., 2003; Serini et al., 1998; White et al., 2008). Here we confirmed that FN B-A+ was able to induce the expression of TGF-β response genes. However, using our complete toolset of purified full-length extra-domain-containing FN variants and FN-deficient fibroblasts we found that effect was most pronounced for the other variants. We further showed that this effect could be attributed to FN-induced activation of latent TGF-β. A series of elegant studies have demonstrated that latent TGF-β can be activated by strain generated within the actin-integrin-ECM axis [reviewed in (Kim et al., 2018)] and involving FN-bound latent TGF-β binding proteins (LTBPs, namely LTBP1 and 3). In our experimental system, TGF-β signaling peaked at 2 h after presenting the variants to the *Fn1* -/- MFs. At this early time point LTBP1 is not likely to be incorporated into nascent FN fibrils (Dallas et al., 2005), suggesting that FN-induced activation of latent TGF-β/TGFβ receptors by fibroblasts could involve a mechanism that operates in absence of a mature matrix.

The computational tools described here allow robust classification of variant-specific fibrillar FN networks. To analyze scale and fiber orientation, we chose to use the Gabor filters over the curvelet transforms (Grapa et al., 2018; Liu et al., 2017) to eliminate complications related to translation and rotation. The fiber centers were identified after establishing the skeletons, and a reconnection or "gap filling" procedure was implemented to generate a more faithful representation of the fiber networks. Remarkably, our findings unequivocally demonstrate that the presence of the extra domains confers quantitatively tractable topological differences to each of the four FN variant networks. These results, together with those of our functional studies, allow us to propose a scenario in which the presence of one or both extra domains in FN, through distinct conformational changes, alters intra- and inter-molecular interactions

that differentially initiate and sustain integrin-mediated signaling events that drive FN fibrillogenesis and a host of cellular responses. Although the cellular responses observed in MFs were modest, availability of extra domain-containing FN should allow further investigations of the specific effects in other cell types.

With the ultimate goal of developing a generative model of cFN networks and tools for image-based tumor biomarker analysis, we chose a scale-space strategy for analysis of fiber geometry. Our graph-based description of the fibers based on Gabor filters was designed to compute and extract statistics about network features. The selected features (fiber orientation, connectivity, thickness, anisotropy, and fiber/pore density) are known to play determinant roles in defining cell migration modes and invasion strategies during tumor progression (Kurniawan et al., 2016; Walker et al., 2018; Wolf and Friedl, 2011), and orienting cell division during tissue expansion and development (Dekoninck et al., 2020). Alignment of collagen fibers is a well-established hallmark of tumor-associated stromal matrix and indicator of poor prognosis (Egeblad et al., 2010; Malik et al., 2015; Provenzano et al., 2006). We and others have shown that alignment of FN fibers by cancer-associated fibroblasts (CAFs) promotes directional migration of cancer cells (Attieh et al., 2017; Erdogan and Webb, 2017; Gopal et al., 2017). In the present study, no significant differences in global FN fiber orientation or anisotropy were detected. This is likely due to the fact that the fibers are deposited by normal, and not activated fibroblasts (myofibroblasts). Networks deposited by MFs presented with plasma-like FN B-A- and B-A+ variants were the most distinguishable. Plasma-like FN networks displayed the greatest fiber heterogeneity, with a highest proportion of unbranched fibers and larger and more elongated pores than the extra domain-containing FN networks. High structural heterogeneity could explain why plasma-like FN matrices displayed the widest distribution of AFM measurements. In contrast, networks of FN containing extra domains, especially FN B-A+, were more branched and displayed smaller pores. Interestingly, the presence of EDB resulted in a mixed set of attributes for which further molecular insights into EDB-specific interactions would be necessary to explain how this occurs. Future work will extend these computational analyses of FN networks assembled by fibroblasts in vitro to the characterization of FN network features in the stroma of human tumors in which cFN overexpression is an independent unfavorable prognostic indicator (Gopal et al., 2017). Given the fundamental importance of cFN-rich matrices in orchestrating matrix organization and regulating the behavior of numerous cellular effectors in the tumor microenvironment [reviewed in (Efthymiou et al., 2020)], the experimental tools and computational resources described here should prove valuable for accelerating biologically- and clinically-relevant discoveries in this field.

Materials and methods

Materials

Human plasma FN was from BD Biosciences (Bedford, MA, USA). All other chemicals and reagents were purchased from Sigma Aldrich (St Louis, MO, USA) unless otherwise stated.

Cells and culture conditions

Human umbilical vein endothelial cells (HUVECs) were prepared from fresh human umbilical veins and maintained as previously described (Radwanska et al., 2017). *Fn1 fl/fl* mouse kidney fibroblasts (MFs) were kindly provided by Dr. Reinhard Fässler [Max Planck Institute, Martinstread, Germany (Sakai et al., 2001)]. The HEK293FT cell line was from Life Technologies (Saint Aubin, France). All cells were cultured in Dulbecco's Modified Eagle's Medium (DMEM) containing L-glutamine (Thermo Fisher Scientific, Waltham, MA, USA) and 10% fetal calf serum (FCS; 5% for signaling experiments) (Biowest, Nuaillé, France) in a humidified incubator at 37°C with 5% CO_2. For experiments, FN was depleted from FCS using gelatin sepharose-4B columns (GE Healthcare, Uppsala, Sweden), and the culture medium was supplemented with Penicillin-Streptomycin 100 U/ml. No coating was performed on culture dishes and coverslips unless otherwise stated. Absence of Mycoplasma sp. contamination was routinely verified by PCR as described elsewhere (Kong et al., 2001).

Antibodies

Primary antibodies are indicated in Table S1. Secondary antibodies coupled to horseradish peroxidase were from Jackson Immunoresearch Labs (West Grove, PA, USA). Fluorescently labeled (Alexa Fluor 488, 564, and 647-conjugated) secondary antibodies were purchased from Thermo Fisher Scientific.

Lentiviral vector construction and production of lentiviral particles

Alternatively spliced FN variants (containing EDA and/or EDB, or no extra domains) with variable region V-89 (also called IIICS) were expressed in the third generation lentiviral vector 2K7 (Suter et al., 2006) under the elongation factor 1 alpha promoter (EF-1α) in HEK293 cells and *Fn1 -/-* MFs.

Full-length cellular *FN1* cDNA was amplified using primers: 5'-CACCTCTCTCCCCCACCGTCTCAACA-3' (forward) and 5'-GATCTTGGCAGAGAGACATGC-3' (reverse) in a two-step RT-PCR with total RNA isolated from HUVECs. Next, *FN1* cDNA was cloned with the pENTR™/D-TOPO® Cloning Kit (Applied Biosystems, Foster City, CA, USA). EDB or EDA domains were inserted or deleted using site-directed mutagenesis to obtain four different constructs (pENTR-FN) corresponding to the following FN variants: FN/EDB-EDA- (FN B-A-), FN/EDB+EDA- (FN B+A-), FN/EDB-EDA+ (FN B-A+), and FN/EDB+EDA+ (FN B+A+). When verified by sequencing, cDNA of each variant was inserted in the 2K7 lentiviral expression vector by recombination

between appropriate sites in pENTR-EF-1α (L4-R1), pENTR-FN variant (L1-L2) and 2K7-BSD vector with a blasticidine resistance gene. Recombination reaction was performed with LR plus clonase (Applied Biosystems, Foster City, CA, USA).

Lentiviral particles were produced by transfecting HEK293FT cells with a mixture composed of a 2K7-FN variant construct (6 µg) and the virus packaging vectors [6.74 µg of p8.92 (VSVG), and 6.74 µg of p8.93 (Gag, Pol)] using Lipofectamine 2000 (Thermo Fisher Scientific) according to the manufacturer's instructions. Virus-containing supernatants were collected 48 h after transfection.

Purification of FN variants

To generate FN-expressing clones for purification of recombinant variants from conditioned medium, HEK293 cells were transduced with virus-containing supernatants and selected with 7.5 µg/ml blasticidine (Invivogen, San Diego, CA, USA). Blasticidine-resistant cells were cloned by limiting dilution with a flow cytometer (FACSAria, BD Biosciences, San Jose, CA, USA) and FN-expressing clones were selected for variant purification based on the level of FN secretion, as assessed by the Human Fibronectin ELISA kit (Abcam, Cambridge, MA, USA).

FN variant purification was performed as described previously with modifications (Akiyama, 2013). Briefly, HEK293 cells expressing FN variants were cultured at confluence in basal culture medium for 2-3 days. Conditioned medium was subsequently collected and centrifuged in the presence of 0.2 mM PMSF. Ten ml of Gelatin-Sepharose® 4B (GE Healthcare) were added per 500 ml of supernatant prior to overnight incubation at 4°C with slight agitation. Eluted FN fractions corresponding to the highest absorbance (A280) were pooled, and FN was subsequently dialyzed against CAPS-saline buffer pH 11.0. FN aliquots were flash frozen and stored at -80°C. The purity and concentration of FN variants were verified using Coomassie Blue gel staining, silver stain, and the Pierce™ BCA Protein Assay Kit (Thermo Fisher Scientific), according to manufacturer's instructions. To assess the presence of insoluble aggregates, glass coverslips were coated with 3 µg/ml of FN variants at 37°C for 1 h then fixed, blocked, and stained for immunofluorescence analysis with an anti-FN antibody. Detection of TGF-β1 in the purified FN preparations was performed with the Quantikine® ELISA Human TGF-β1 Immunoassay Kit (R&D Systems, Minneapolis, MN, USA), according to the manufacturer's instructions. Low or no expression of other potentially contaminating factors of the PDGF, FGF, VEGF and TGF-β families (Martino and Hubbell, 2010) by these cells was verified by using the Human Protein Atlas database (https://www.proteinatlas.org/humanproteome/cell, retrieved on November 10, 2020).

Knockout of FN in *Fn1 fl/fl* mouse fibroblasts and re-expression of FN variants

Cre recombination was performed by infecting *Fn1 fl/fl* MFs with a self-excising Cre retrovirus [pMMP-RV-Cre-GFP (Silver and Livingston, 2001)] and transduced cells were selected with 6.5 μg/ml puromycin. Clones were obtained by limiting dilution with a flow cytometer and analyzed for FN expression and gene deletion by immunofluorescence staining and PCR analysis, respectively.

MFs expressing FN variants, were generated by infection of *Fn1 -/-* clone D MFs with viral supernatants, as described above. Transduced cells were selected in the presence of 7.5 μg/mL blasticidine + 6.5 μg/ml puromycin and cloned by limiting dilution with a flow cytometer. Stable FN variant-expressing clones were selected for analysis based on FN expression levels, as assessed by immunofluorescence staining.

RNA isolation, reverse transcription, and qRT-PCR

Cells were lysed with Trizol reagent (Thermo Fisher Scientific) according to the manufacturer's instructions. RNA samples were quantified using a small-volume spectrophotometer (DeNovix DS-11 series, Wilmington, DE, USA) and 1 μg of RNA was reverse-transcribed into cDNA using the High-Capacity cDNA Reverse Transcription Kit (Thermo Fisher Scientific). The resulting cDNA was diluted tenfold and amplified in a StepOne Plus thermocycler (Thermo Fisher Scientific) using gene-specific primers and PowerUp™ SYBR™ Green Master Mix (Thermo Fisher Scientific). Standard cycling conditions were used. For FN re-expression, results are represented by the -ΔCt values ($Ct_{\text{gene of interest}} - Ct_{\text{normalizing gene}}$) as arbitrary units (AU). For FN stimulation experiments, results were analyzed according to the $2^{-\Delta\Delta Ct}$ method and are expressed as fold change compared to vehicle control (CTRL). *Tbp* was used as the normalizing gene. Primer sequences are indicated in Table S2.

Western blotting

Whole cell lysates and conditioned media were collected with Laemmli buffer 3x (6% SDS, 30% glycerol, 187.5 mM Tris HCl pH 6.8) under non-reducing or reducing conditions (5% β-mercaptoethanol), separated by gel electrophoresis and transferred onto Immobilon P membranes (Millipore, Bedford, MA, USA). Membranes were blocked with 3% skim milk in TBS (50 mM Tris-HCl pH 7.4; 150 mM NaCl) before protein immunodetection with the indicated antibodies (Supplemental Table 1). Protein bands were visualized with horseradish peroxidase (HRP)-conjugated secondary antibodies followed by enhanced chemiluminescence (Bio-Rad, Hercules, CA, USA) in a Fusion Fx7 Advanced system (Vilber Lourmat, Eberhardzell, Germany).

Immunofluorescence staining and microscopy

For immunofluorescence analyses, cells or decellularized matrices were fixed in 4% paraformaldehyde with 3% sucrose and permeabilized with 0.2% Triton X-100. The dilutions of the primary and secondary antibodies are shown in Table S1. Nuclei were detected with Hoechst 33342 (Thermo Fisher Scientific). After staining, the coverslips were mounted in ProLong® Gold antifade reagent (Thermo Fischer Scientific). Widefield fluorescence was observed through 40X/1.3 NA or 63X/1.4 NA oil objectives on a Zeiss Axiovert 200M microscope equipped with a CoolSnap HQ CCD. Image acquisition was performed using the MetaMorph Imaging System. Confocal imaging was performed on a Zeiss LSM710 confocal system using 10X/0.45 NA and 63X/1.4 NA objectives. Image analysis was performed using Fiji (Schindelin et al., 2012).

Proliferation rate and cell doubling time

Fn1 -/- MFs were plated in triplicate at a density of $2.5X10^4$ cells/well in 24-well plates. Cells were stimulated after 3-4 h with 15 µg/ml of recombinant FN variants, or vehicle buffer (CAPS-saline). At the indicated times, cells were trypsinized, resuspended in culture medium and counted with a Malassez hemocytometer (Thermo Fisher Scientific). Cell doubling time was determined during the exponential phase of growth (between days 2 and 3) in control and variant-treated cells by using the reverse equation and the "Goal-Seek" function in MS Excel.

Internal pH measurement

Fn1 -/- MFs were plated in duplicates in 24-well plates ($5X10^4$ cells/well). Cells were stimulated with 15 µg/ml of recombinant FN variants, or vehicle buffer (CAPS-saline) for 48 h. Internal pH (pHi) measurement was performed as described (Cophignon et al., 2017). Briefly, cells were incubated with 1 µM BCECF-AM (Thermo Fisher Scientific) for 1 h, rinsed with recovery solution (120 mM sodium chloride, 5 mM KCl, 1 mM $MgCl_2$, 2 mM $CaCl_2$, 5 mM glucose, 15 mM Hepes), and fluorescence intensity was measured using a multi-well plate spectrophotometer (BioTek Synergy 4, Winooski, VT, USA). Data were collected with the integrated software. Recovery solution was removed, and nigericin solutions were added (140 mM KCl, 1 mM $MgCl_2$, 2 mM $CaCl_2$, 5 mM glucose, 5 µM nigericin at pH values ranging from 6.5 to 8.0 in the presence of 20 mM Hepes).

Mitochondrial metabolism and glycolytic measurements

For metabolic analysis, cells were seeded in 24-well plates (Seahorse Bioscience, Billerica, MA) and stimulated with 15 µg/ml of recombinant FN variants or vehicle buffer for 48 h. The oxygen consumption rate (OCR) and extracellular acidification rate (ECAR) were determined using an XF24 Extracellular Flux Analyzer (Seahorse Bioscience) and Seahorse basal medium supplemented with 2 mM glutamine. Maximal OCR was determined by using FCCP (1 µM), and rotenone and antimycin-A (2 µM each) were

used to inhibit Complex I- and Complex III-dependent respiration, respectively. All parameters were calculated as described previously (Brand and Nicholls, 2011).

For glucose uptake comparison, *Fn1 -/-* MFs were plated in triplicates in 96-well plates ($4X10^3$ cells/well) and stimulated with 15 µg/ml of FN variants or vehicle buffer for 48 h. Cells were washed with PBS, starved with glucose-depleted medium for 30 min before adding 200 µM of 2-NBDG (Thermo Fisher Scientific) for 40 min. Fluorescence intensity was measured in a microplate reader (BioTek Synergy 4). Results are represented as fold difference relative to CTRL. Lactate extrusion in the culture medium of *Fn1 -/-* MFs treated with FN variants for 48 h (same conditions as in proliferation rate experiments) was analyzed using a Dionex ion chromatography column (Thermo Fisher Scientific).

Generation of MF-derived matrices

MF-derived matrices were generated as described previously (Kaukonen et al., 2016). Briefly, coverslips were coated with 0.2% gelatin for 60 min at 37°C, followed by crosslinking with 1% glutaraldehyde for 30 min at room temperature. Crosslinker was quenched with 1 M glycine for 20 min and gelatin-coated coverslips were incubated with medium before seeding $2X10^5$ cells. Ascorbic acid (50 µg/ml) and FN variants (15 µg/ml) were added the next day. On day 3, medium was changed, and on day 7, matrices were decellularized in 20 mM NH_4OH, 0.5% Triton X-100 in PBS followed by 10 µM DNase I treatment (Roche Diagnostics GmbH, Penzberg, Germany).

Atomic Force microscopy

Decellularized ECM was prepared on 35mm dishes. Samples were rinsed and immersed in 3 ml of PBS. The mechanical properties of the samples were studied as described previously (Andersen et al., 2019) with slight modifications. Briefly, four areas per sample were analyzed, and 140 force-distance curves were collected. Deflection sensitivity and spring constant of the cantilever were determined using a clean glass dish with PBS. Velocity and trigger threshold were set to 1 µm/s and 2 nN respectively. The elastic (Young's) modulus was calculated as described previously. To eliminate any tilt effect due to the base correction step in the analysis, only force curves with maximum value equal to 2 nN were used to perform the fit.

Collagen gel contraction assay

Fn1 -/- MFs were embedded ($20X10^4$ cells/lattice) in collagen lattices (1 mg/ml) containing 15 µg/ml of FN variants in duplicates in 12-well plates. A corresponding volume of NaOH was added to bring the pH of the mixture back to 7.4 and lattices were left at room temperature for 30 min to solidify. Medium

containing 15 μg/ml of FN variants was added on top of the lattices which were subsequently detached from the well walls and bottom. Gel surface reduction was measured with ImageJ after a 24-hour incubation at 37°C in the presence of 5% CO_2.

Computational analysis of matrix topology

Image Acquisition for numerical characterization of FN variant fibers and classification

Confocal images of 3128 × 3128 pixels with a lateral resolution of 0.27 μm/pixel were acquired with a Zeiss LSM710 confocal system with a 10X/0.45 Na objective with the pinhole diameter set to its maximal value. For each FN variant, 70 images corresponding to a representative region of 512 × 512 pixels were selected for feature extraction and classification. The set of 280 gray-scale images was classified with the GoogLeNet (Szegedy et al., 2015) pretrained Convolutional Neural Net (CNN) architecture using the MATLAB Deep Learning Toolbox and a 22-layer deep network trained on more than 1 million images for classification into 1000 object categories. A set of 196 images was used for the training of the algorithm, and the remaining 84 for testing it. The training image set was presented to the algorithm 25 times (epochs) as described (Ruder, 2017), to improve classification accuracy.

Definition of Gabor kernels

Fibrillar structures were detected and enhanced with Gabor filters (Petkov, 1995), commonly employed in image processing for the detection of structures with different frequencies, and certain directionalities. A set of Gabor kernels was defined, characterized by the formula

$$G_{\theta_i,\lambda_j,\varphi,\sum_{\theta_i}}(\mathrm{x},\mathrm{y}) = \exp\left(-\frac{1}{2}v^t\sum_{\theta_i}^{-1}v\right)\cos\left(\frac{2\pi x\theta_i}{\lambda_j}+\varphi\right) \quad (1),$$

where $v=(x,y)^t$. The exponential term provides the shape of a bivariate Gaussian kernel, and the cosine function describes its oscillations in space, while v is the 2D coordinate vector, indicating pixel localization in a bi-dimensional Cartesian coordinate system.

Fiber detection computation and morphological skeletonization

Fiber orientation was represented by θ_i with values within the interval $[0,\pi]$, with a stepsize of $\frac{\pi}{20}$. The covariance matrix of the bivariate Gaussian function rotated with θ_i is related to the anisotropy of the kernel spatial support and is designated by $\sum_{\theta_i}$. Fiber thickness is represented by λ_j that corresponds to the wavelength (in pixels) of the cosine term, the values of which are equal to $\frac{\lambda_j}{2}$ and vary between 3 and 5 pixels. The thinnest fibers are detected when $\lambda_j = 6$ pixels, medium thickness fibers correspond to $\lambda_j =$

8 pixels, while the thickest are characterized by $\lambda_j = 10$ pixels. For accurate localization of fibers we used phase, φ, set to 0. The pixel intensity of a detected fiber at a specific location corresponded to the Gabor filter with the highest coefficient within the Gabor kernel set. The specific parameters of the best corresponding Gabor kernel for a detected fiber could subsequently be linked to physical properties, such as fiber thickness and local fiber orientation.

Morphological skeletons of the detected fibers were computed using morphological operations provided by the Image Processing Toolbox of MATLAB 2015a. Fiber skeletons were portrayed as graph-based representations in which a set of nodes is linked by edges (connecting segments), using a toolbox (Kollmannsberger et al., 2017) that generates the network graph of a 3D skeleton voxel, that we adapted to the 2D setting. Nodes typically represent intersecting fibers or fiber ends, while edges correspond to the detected fibers connecting the nodes.

Feature extraction and Principal Component Analysis (PCA)

Features related to fiber thickness and connectivity were directly computed using Gabor kernels and graph-specific parameters. More specifically, connectivity was defined as the proportion of degree 1 nodes (those corresponding to fiber ends) relative to the nodes with a degree higher than 2 (corresponding to branching and intersecting points). Fiber thickness kurtosis, was determined by the formula

$$k = E[(x-\mu)^4]/(\sigma^4) \quad (2),$$

where μ is the mean value of x, σ is the standard deviation of x, and $E[s]$ is the expected value of the quantity s. Attributes describing pore regions were computed using the MATLAB tool Regionprops. Pore dimension was measured as the total number of pixels within the area delimited by the skeleton, while pore circularity was determined by the formula

$$(4 * Area * \pi)/(Perimeter^2) \quad (3),$$

the values of which vary between 0 (line-like) and 1 (perfect circle). For pore size, only pores distributed above the 90th percentile were taken into account, and the mean was calculated. For PCA visualization, each FN network sample (image) was represented in a 5-dimensional space defined by the previously selected features.

Statistical Analysis

Values are represented as the mean ±s.e.m. when n≥3 and as mean ±s.d. when n=2, where n is the number of independent experiments (specified in Fig. legends) unless otherwise stated. Statistical significance was assessed by two-tailed Student's *t test* using Microsoft Excel for Windows (function *t test*). The Kruskal-Wallis test for non-parametric distributions, followed by a Dunn's multiple comparison test was applied for statistical analysis of AFM using GraphPad Prism v5.03 for Windows. *P* value is represented by asterisks: * $P \leq 0.05$; ** $P \leq 0.01$; *** $P \leq 0.001$; **** $P \leq 0.0001$. Asterisks above bars represent significance between the respective condition and the CTRL. Asterisks above horizontal brackets represent the significance between the conditions at each end of the bracket.

Acknowledgements

We gratefully acknowledge Agnès Loubat (iBV cytometry facility) for cell sorting, the iBV PRISM imaging and protein purification facilities and the PICMI imaging facility of IRCAN. We thank Karl-Hans Kraus (University of Geneva) and Thierry Virolle (Université Côte d'Azur) for lentiviral vectors and Reinhard Fässler (Max Planck Institute of Biochemistry) for floxed MFs, Michel Tauc for anion profiling experiments and Emmanuel Van Obberghen for critical review of the manuscript.

Competing interests

The authors declare that there are no competing interests.

Funding

Support for this work was provided by the National Agency for Research (ANR-16-CE93-0005-01), the LabEx SIGNALIFE program (ANR-11-LABX-0028-01), the Fondation ARC (PJA20151203207, fellowship GE). EVO team members are affiliated to the Fédération Hospitalo-Universitaire OncoAge. EVO and LBF hold Chairs, 3IA Côte d'Azur (ANR-19-P3IA-0002).

Author contributions: EVOS conceived the project, established collaborations, analyzed the data, and acquired funding for the work. The manuscript was written by EVOS and GE, reviewed and edited by all authors. AR designed and generated the molecular tools. GE, AR, SBFD and DG performed experiments involving molecular, cellular and biochemical analyses, contributed to the experimental design and data analysis. MH, GE, AR and DG purified the recombinant proteins. AG, XD and LBF developed the computational tools and implemented numerical analyses of images. SS developed software and contributed to image analysis. MP, DP and LC provided expertise, performed experiments and analyzed data involving pH regulation and metabolism. SP performed AFM experiments and data analysis.

Materials and data sharing: All data needed to evaluate the conclusions in the paper are present in the paper and/or the Supplementary Information. All reagents, data, and computer code for this study are available upon request from the authors.

References and Notes

Akiyama, S. K. (2013). Purification of Fibronectin. *Current Protocols in Cell Biology* **60**, 10.5.1-10.5.13.

Alkasalias, T., Moyano-Galceran, L., Arsenian-Henriksson, M. and Lehti, K. (2018). Fibroblasts in the Tumor Microenvironment: Shield or Spear? *IJMS* **19**, 1532.

Andersen, M. S., Hannezo, E., Ulyanchenko, S., Estrach, S., Antoku, Y., Pisano, S., Boonekamp, K. E., Sendrup, S., Maimets, M., Pedersen, M. T., et al. (2019). Tracing the cellular dynamics of sebaceous gland development in normal and perturbed states. *Nat Cell Biol* **21**, 924–932.

Arslan, F., Smeets, M. B., Riem Vis, P. W., Karper, J. C., Quax, P. H., Bongartz, L. G., Peters, J. H., Hoefer, I. E., Doevendans, P. A., Pasterkamp, G., et al. (2011). Lack of Fibronectin-EDA Promotes Survival and Prevents Adverse Remodeling and Heart Function Deterioration After Myocardial Infarction. *Circ Res* **108**, 582–592.

Astrof, S., Crowley, D. and Hynes, R. O. (2007). Multiple cardiovascular defects caused by the absence of alternatively spliced segments of fibronectin. *Developmental Biology* **311**, 11–24.

Attieh, Y., Clark, A. G., Grass, C., Richon, S., Pocard, M., Mariani, P., Elkhatib, N., Betz, T., Gurchenkov, B. and Vignjevic, D. M. (2017). Cancer-associated fibroblasts lead tumor invasion through integrin-β3–dependent fibronectin assembly. *J Cell Biol* **216**, 3509–3520.

Balza, E., Borsi, L., Allemanni, G. and Zardi, L. (1988). Transforming growth factor β regulates the levels of different fibronectin isoforms in normal human cultured fibroblasts. *FEBS Letters* **228**, 42–44.

Balza, E., Sassi, F., Ventura, E., Parodi, A., Fossati, S., Blalock, W., Carnemolla, B., Castellani, P., Zardi, L. and Borsi, L. (2009). A novel human fibronectin cryptic sequence unmasked by the insertion of the angiogenesis-associated extra type III domain B. *Int. J. Cancer* **125**, 751–758.

Bass, M. D., Roach, K. A., Morgan, M. R., Mostafavi-Pour, Z., Schoen, T., Muramatsu, T., Mayer, U., Ballestrem, C., Spatz, J. P. and Humphries, M. J. (2007). Syndecan-4–dependent Rac1 regulation determines directional migration in response to the extracellular matrix. *Journal of Cell Biology* **177**, 527–538.

Booth, A. J., Wood, S. C., Cornett, A. M., Dreffs, A. A., Lu, G., Muro, A. F., White, E. S. and Bishop, D. K. (2012). Recipient-derived EDA fibronectin promotes cardiac allograft fibrosis. *J. Pathol.* **226**, 609–618.

Borsi, L., Castellani, P., Risso, A. M., Leprini, A. and Zardi, L. (1990). Transforming growth factor-β regulates the splicing pattern of fibronectin messenger RNA precursor. *FEBS Letters* **261**, 175–178.

Brand, M. D. and Nicholls, D. G. (2011). Assessing mitochondrial dysfunction in cells. *Biochem. J.* **435**, 297–312.

Carnemolla, B., Leprini, A., Allemanni, G., Saginatti, M. and Zardi, L. (1992). The inclusion of the type III repeat ED-B in the fibronectin molecule generates conformational modifications that unmask a cryptic sequence. *Journal of Biological Chemistry* **267**, 24689–24692.

Castellani, P. (1986). Transformed human cells release different fibronectin variants than do normal cells. *The Journal of Cell Biology* **103**, 1671–1677.

Castelletti, F., Donadelli, R., Banterla, F., Hildebrandt, F., Zipfel, P. F., Bresin, E., Otto, E., Skerka, C., Renieri, A., Todeschini, M., et al. (2008). Mutations in FN1 cause glomerulopathy with fibronectin deposits. *Proceedings of the National Academy of Sciences* **105**, 2538–2543.

Cophignon, A., Poët, M., Monet, M., Tauc, M. and Counillon, L. (2017). CD95-Mediated Proton Regulation. In *CD95* (ed. Legembre, P.), pp. 95–102. New York, NY: Springer New York.

Cseh, B., Fernandez-Sauze, S., Grall, D., Schaub, S., Doma, E. and Van Obberghen-Schilling, E. (2010). Autocrine fibronectin directs matrix assembly and crosstalk between cell-matrix and cell-cell adhesion in vascular endothelial cells. *Journal of Cell Science* **123**, 3989–3999.

Dallas, S. L., Sivakumar, P., Jones, C. J. P., Chen, Q., Peters, D. M., Mosher, D. F., Humphries, M. J. and Kielty, C. M. (2005). Fibronectin Regulates Latent Transforming Growth Factor-β (TGFβ) by Controlling Matrix Assembly of Latent TGFβ-binding Protein-1. *J. Biol. Chem.* **280**, 18871–18880.

Dekoninck, S., Hannezo, E., Sifrim, A., Miroshnikova, Y. A., Aragona, M., Malfait, M., Gargouri, S., de Neunheuser, C., Dubois, C., Voet, T., et al. (2020). Defining the Design Principles of Skin Epidermis Postnatal Growth. *Cell* S0092867420302774.

Efthymiou, G., Saint, A., Ruff, M., Rekad, Z., Ciais, D. and Van Obberghen-Schilling, E. (2020). Shaping Up the Tumor Microenvironment With Cellular Fibronectin. *Front. Oncol.* **10**, 641.

Egeblad, M., Rasch, M. G. and Weaver, V. M. (2010). Dynamic interplay between the collagen scaffold and tumor evolution. *Current Opinion in Cell Biology* **22**, 697–706.

Erdogan, B. and Webb, D. J. (2017). Cancer-associated fibroblasts modulate growth factor signaling and extracellular matrix remodeling to regulate tumor metastasis. *Biochm. Soc. Trans.* **45**, 229–236.

Ffrench-Constant, C. (1989). Reappearance of an embryonic pattern of fibronectin splicing during wound healing in the adult rat. *The Journal of Cell Biology* **109**, 903–914.

Fontana, L., Chen, Y., Prijatelj, P., Sakai, T., Fässler, R., Sakai, L. Y. and Rifkin, D. B. (2005). Fibronectin is required for integrin αvβ6-mediated activation of latent TGF-β complexes containing LTBP-1. *The FASEB Journal* **19**, 1798–1808.

Frantz, C., Stewart, K. M. and Weaver, V. M. (2010). The extracellular matrix at a glance. *Journal of Cell Science* **123**, 4195–4200.

Fukuda, T., Yoshida, N., Kataoka, Y., Manabe, R., Mizuno-Horikawa, Y., Sato, M., Kuriyama, K., Yasui, N. and Sekiguchi, K. (2002). Mice Lacking the EDB Segment of Fibronectin Develop Normally but Exhibit Reduced Cell Growth and Fibronectin Matrix Assembly in Vitro. *Cancer Research* **62**, 5603–5610.

George, E. L., Georges-Labouesse, E. N., Patel-King, R. S., Rayburn, H. and Hynes, R. O. (1993). Defects in mesoderm, neural tube and vascular development in mouse embryos lacking fibronectin. *Development* **119**, 1079–1091.

Goetz, J. G., Minguet, S., Navarro-Lérida, I., Lazcano, J. J., Samaniego, R., Calvo, E., Tello, M., Osteso-Ibáñez, T., Pellinen, T., Echarri, A., et al. (2011). Biomechanical Remodeling of the Microenvironment by Stromal Caveolin-1 Favors Tumor Invasion and Metastasis. *Cell* **146**, 148–163.

Gopal, S., Veracini, L., Grall, D., Butori, C., Schaub, S., Audebert, S., Camoin, L., Baudelet, E., Radwanska, A., Beghelli-de la Forest Divonne, S., et al. (2017). Fibronectin-guided migration of carcinoma collectives. *Nat Commun* **8**, 14105.

Grapa, A.-I., Meunier, R., Blanc-Feraud, L., Efthymiou, G., Schaub, S., Radwanska, A., van Obberghen-Schilling, E. and Descombes, X. (2018). Classification of the fibronectin variants with curvelets. In *2018 IEEE 15th International Symposium on Biomedical Imaging (ISBI 2018)*, pp. 930–933. Washington, DC: IEEE.

Guan, J. L., Trevithick, J. E. and Hynes, R. O. (1990). Retroviral expression of alternatively spliced forms of rat fibronectin. *The Journal of Cell Biology* **110**, 833–847.

Henderson, N., Arnold, T., Katamura, Y. et al. (2013). Targeting of αv integrin identifies a core molecular pathway that regulates fibrosis in several organs. *Nat Med* **19,** 1617–1624

Hinz, B. (2015). The extracellular matrix and transforming growth factor-β1: Tale of a strained relationship. *Matrix Biology* **47**, 54–65.

Hirshoren, N., Kohan, M., Assayag, M., Neuman, T., Vernea, F., Muro, A., Eliashar, R. and Berkman, N. (2013). Extra domain-A fibronectin is necessary for the development of nasal remodeling in chronic allergen-induced rhinitis. *Annals of Allergy, Asthma & Immunology* **110**, 322–327.

Hynes, R. O. (1990). *Fibronectins*. New York, NY: Springer New York.

Hynes, R. O. (2009). The Extracellular Matrix: Not Just Pretty Fibrils. *Science* **326**, 1216–1219.

Hynes, R. O. and Naba, A. (2012). Overview of the Matrisome--An Inventory of Extracellular Matrix Constituents and Functions. *Cold Spring Harbor Perspectives in Biology* **4**, a004903–a004903.

Ignotz, R. A. and Massagué, J. (1986). Transforming GrowthFactor-@Stimulates the Expression of Fibronectin and Collagen and Their Incorporatiointo the Extracellular Matrix. *The Journal of Biological Chemistry* **261**, 4337–4345.

Ignotz, R. A. and Massagué, J. (1987). Cell adhesion protein receptors as targets for transforming growth factor-β action. *Cell* **51**, 189–197.

Kaukonen, R., Mai, A., Georgiadou, M., Saari, M., De Franceschi, N., Betz, T., Sihto, H., Ventelä, S., Elo, L., Jokitalo, E., et al. (2016). Normal stroma suppresses cancer cell proliferation via mechanosensitive regulation of JMJD1a-mediated transcription. *Nat Commun* **7**, 12237.

Kim, K. K., Sheppard, D. and Chapman, H. A. (2018). TGF-β1 Signaling and Tissue Fibrosis. *Cold Spring Harb Perspect Biol* **10**, a022293.

Kohan, M., Muro, A. F., Bader, R. and Berkman, N. (2011). The extra domain A of fibronectin is essential for allergen-induced airway fibrosis and hyperresponsiveness in mice. *Journal of Allergy and Clinical Immunology* **127**, 439-446.e5.

Kollmannsberger, P., Kerschnitzki, M., Repp, F., Wagermaier, W., Weinkamer, R. and Fratzl, P. (2017). The small world of osteocytes: connectomics of the lacuno-canalicular network in bone. *New J. Phys.* **19**, 073019.

Kong, F., James, G., Gordon, S., Zelynski, A. and Gilbert, G. L. (2001). Species-Specific PCR for Identification of Common Contaminant Mollicutes in Cell Culture. *Applied and Environmental Microbiology* **67**, 3195–3200.

Kurniawan, N. A., Chaudhuri, P. K. and Lim, C. T. (2016). Mechanobiology of cell migration in the context of dynamic two-way cell–matrix interactions. *Journal of Biomechanics* **49**, 1355–1368.

Kutz, S. M., Hordines, J., McKeown-Longo, P. J. and Higgins, P. J. (2001). TGF-β1-induced PAI-1 gene expression requires MEK activity and cell-to-substrate adhesion. *Journal of Cell Science* **114**, 3905–3914.

Leask, A. and Abraham, D. J. (2003). The role of connective tissue growth factor, a multifunctional matricellular protein, in fibroblast biology. *Biochem. Cell Biol.* **81**, 355–363.

Liu, Y., Keikhosravi, A., Mehta, G. S., Drifka, C. R. and Eliceiri, K. W. (2017). Methods for Quantifying Fibrillar Collagen Alignment. In *Fibrosis* (ed. Rittié, L.), pp. 429–451. New York, NY: Springer New York.

Malik, R., Lelkes, P. I. and Cukierman, E. (2015). Biomechanical and biochemical remodeling of stromal extracellular matrix in cancer. *Trends in Biotechnology* **33**, 230–236.

Manabe, R., Oh-e, N. and Sekiguchi, K. (1999). Alternatively Spliced EDA Segment Regulates Fibronectin-dependent Cell Cycle Progression and Mitogenic Signal Transduction. *J. Biol. Chem.* **274**, 5919–5924.

Martino, M. M. and Hubbell, J. A. (2010). The 12th–14th type III repeats of fibronectin function as a highly promiscuous growth factor-binding domain. *The FASEB Journal* **24**, 4711–4721.

Mezzenga, R. and Mitsi, M. (2019). The Molecular Dance of Fibronectin: Conformational Flexibility Leads to Functional Versatility. *Biomacromolecules* **20**, 55–72.

Muro, A. F., Chauhan, A. K., Gajovic, S., Iaconcig, A., Porro, F., Stanta, G. and Baralle, F. E. (2003). Regulated splicing of the fibronectin EDA exon is essential for proper skin wound healing and normal lifespan. *J Cell Biol* **162**, 149–160.

Ohashi, T. and Erickson, H. P. (2011). Fibronectin Aggregation and Assembly: THE UNFOLDING OF THE SECOND FIBRONECTIN TYPE III DOMAIN. *J. Biol. Chem.* **286**, 39188–39199.

Ohashi, T., Kiehart, D. P. and Erickson, H. P. (1999). Dynamics and elasticity of the fibronectin matrix in living cell culture visualized by fibronectin-green fluorescent protein. *Proceedings of the National Academy of Sciences* **96**, 2153–2158.

Ohashi, T., Kiehart, D. P. and Erickson, H. P. (2002). Dual labeling of the fibronectin matrix and actin cytoskeleton with green fluorescent protein variants. *Journal of Cell Science* **115**, 1221–1229.

Pavlides, S., Whitaker-Menezes, D., Castello-Cros, R., Flomenberg, N., Witkiewicz, A. K., Frank, P. G., Casimiro, M. C., Wang, C., Fortina, P., Addya, S., et al. (2009). The reverse Warburg effect: Aerobic glycolysis in cancer associated fibroblasts and the tumor stroma. *Cell Cycle* **8**, 3984–4001.

Petkov, N. (1995). Biologically motivated computationally intensive approaches to image pattern recognition. *Future Generation Computer Systems* **11**, 451–465.

Provenzano, P. P., Eliceiri, K. W., Campbell, J. M., Inman, D. R., White, J. G. and Keely, P. J. (2006). Collagen reorganization at the tumor-stromal interface facilitates local invasion. *BMC Med* **4**, 38.

Radwanska A, Grall D, Schaub S, Beghelli-de la Forest Divonne S, Ciais D, Rekima S, Rupp T, Sudaka A, Orend G, Van Obberghen-Schilling E. (2017). Counterbalancing anti-adhesive effects of Tenascin-C through fibronectin expression in endothelial cells. *Sci Rep.* **7**, 12762.

Ruder, S. (2017). An overview of gradient descent optimization algorithms. *arXiv:1609.04747 [cs]*.

Sakai, T., Johnson, K. J., Murozono, M., Sakai, K., Magnuson, M. A., Wieloch, T., Cronberg, T., Isshiki, A., Erickson, H. P. and Fässler, R. (2001). Plasma fibronectin supports neuronal survival and reduces brain injury following transient focal cerebral ischemia but is not essential for skin-wound healing and hemostasis. *Nat Med* **7**, 324–330.

Sarrazy, V., Koehler, A., Chow, M. L., Zimina, E., Li, C. X., Kato, H., Caldarone, C. A. and Hinz, B. (2014). Integrins αvβ5 and αvβ3 promote latent TGF-β1 activation by human cardiac fibroblast contraction. *Cardiovascular Research* **102**, 407–417.

Schiefner, A., Gebauer, M. and Skerra, A. (2012). Extra-domain B in Oncofetal Fibronectin Structurally Promotes Fibrillar Head-to-tail Dimerization of Extracellular Matrix Protein. *J. Biol. Chem.* **287**, 17578–17588.

Schindelin, J., Arganda-Carreras, I., Frise, E., Kaynig, V., Longair, M., Pietzsch, T., Preibisch, S., Rueden, C., Saalfeld, S., Schmid, B., et al. (2012). Fiji: an open-source platform for biological-image analysis. *Nat Methods* **9**, 676–682.

Schwarzbauer, J. E. (1991). Alternative splicing of fibronectin: Three variants, three functions. *Bioessays* **13**, 527–533.

Serini, G., Bochaton-Piallat, M.-L., Ropraz, P., Geinoz, A., Borsi, L., Zardi, L. and Gabbiani, G. (1998). The Fibronectin Domain ED-A Is Crucial for Myofibroblastic Phenotype Induction by Transforming Growth Factor-☒. *The Journal of Cell Biology* **142**, 9.

Silver, D. P. and Livingston, D. M. (2001). Self-Excising Retroviral Vectors Encoding the Cre Recombinase Overcome Cre-Mediated Cellular Toxicity. *Molecular Cell* **8**, 233–243.

Singh, P., Carraher, C. and Schwarzbauer, J. E. (2010). Assembly of Fibronectin Extracellular Matrix. *Annu. Rev. Cell Dev. Biol.* **26**, 397–419.

Sottile, J. and Hocking, D. C. (2002). Fibronectin Polymerization Regulates the Composition and Stability of Extracellular Matrix Fibrils and Cell-Matrix Adhesions. *MBoC* **13**, 3546–3559.

Suter, D. M., Cartier, L., Bettiol, E., Tirefort, D., Jaconi, M. E., Dubois-Dauphin, M. and Krause, K.-H. (2006). Rapid Generation of Stable Transgenic Embryonic Stem Cell Lines Using Modular Lentivectors. *Stem Cells* **24**, 615–623.

Szegedy, C., Wei Liu, Yangqing Jia, Sermanet, P., Reed, S., Anguelov, D., Erhan, D., Vanhoucke, V. and Rabinovich, A. (2015). Going deeper with convolutions. In *2015 IEEE Conference on Computer Vision and Pattern Recognition (CVPR)*, pp. 1–9. Boston, MA, USA: IEEE.

Theocharis, A. D., Skandalis, S. S., Gialeli, C. and Karamanos, N. K. (2016). Extracellular matrix structure. *Advanced Drug Delivery Reviews* **97**, 4–27.

Velling, T., Risteli, J., Wennerberg, K., Mosher, D. F. and Johansson, S. (2002). Polymerization of Type I and III Collagens Is Dependent On Fibronectin and Enhanced By Integrins $\alpha_{11}\beta_1$ and $\alpha_2\beta_1$. *J. Biol. Chem.* **277**, 37377–37381.

Ventura, E., Sassi, F., Parodi, A., Balza, E., Borsi, L., Castellani, P., Carnemolla, B. and Zardi, L. (2010). Alternative Splicing of the Angiogenesis Associated Extra-Domain B of Fibronectin Regulates the Accessibility of the B-C Loop of the Type III Repeat 8. *PLoS ONE* **5**, e9145.

Ventura, E., Cordazzo, C., Quarto, R., Zardi, L. and Rosano, C. (2016). C6: A Monoclonal Antibody Specific for a Fibronectin Epitope Situated at the Interface between the Oncofoetal Extra-Domain B and the Repeat III8. *PLoS ONE* **11**, e0148103.

Vogel, V. (2006). Mechanotransduction involving multimodular proteins: Converting Force into Biochemical Signals. *Annu. Rev. Biophys. Biomol. Struct.* **35**, 459–488.

Walker, C., Mojares, E. and del Río Hernández, A. (2018). Role of Extracellular Matrix in Development and Cancer Progression. *IJMS* **19**, 3028.

Ween, M. P., Oehler, M. K. and Ricciardelli, C. (2012). Transforming Growth Factor-Beta-Induced Protein (TGFBI)/(βig-H3): A Matrix Protein with Dual Functions in Ovarian Cancer. *IJMS* **13**, 10461–10477.

White, E., Baralle, F. and Muro, A. (2008). New insights into form and function of fibronectin splice variants. *J. Pathol.* **216**, 1–14.

Wipff, P.-J., Rifkin, D. B., Meister, J.-J. and Hinz, B. (2007). Myofibroblast contraction activates latent TGF-β1 from the extracellular matrix. *Journal of Cell Biology* **179**, 1311–1323.

Wolf, K. and Friedl, P. (2011). Extracellular matrix determinants of proteolytic and non-proteolytic cell migration. *Trends in Cell Biology* **21**, 736–744.

Yamada, K., Olden, K. (1978). Fibronectins—adhesive glycoproteins of cell surface and blood. *Nature* **275,** 179–184.

Yoshida, G. J. (2015). Metabolic reprogramming: the emerging concept and associated therapeutic strategies. *J Exp Clin Cancer Res* **34**, 111.

Yusuf, B., Gopurappilly, R., Dadheech, N., Gupta, S., Bhonde, R. and Pal, R. (2013). Embryonic fibroblasts represent a connecting link between mesenchymal and embryonic stem cells. *Develop. Growth Differ.* **55**, 330–340.

Figure Legends

Fig. 1. FN variant-expressing MFs. (**A**) Schematic representation of the four human FN variants harboring the EDB and/or EDA (or none), including the variable region V-89, and their expression in assembly competent *Fn1 -/-* MF clones. (**B**) Mean ±s.e.m. FN mRNA levels across selected clones [indicated in (D)] after 7 days in culture, expressed in arbitrary units (AU, n = 3). (**C**) Western analysis of FN expression in four selected clones [same as in (B)] after 7 days in culture (n = 2 independent experiments performed under identical conditions). Numbers beneath the conditioned medium (CM) and cell lysate blots represent the mean ±s.d. fold FN levels relative to MF B-A- in the conditioned medium and cell lysates, respectively. ERK1/2 was used as loading control. The mean ±s.d. ratios of FN in CM to the respective cell associated FN is shown below (n = 2 independent experiments performed under identical conditions). (**D**) Immunofluorescence staining to assess FN re-expression and assembly in the indicated set of clones after 7 days in culture (representative images of n=5 independent experiments are displayed). Nuclei staining is shown in the inserts. Scale bar: 50 μm.

Fig. 2. Presentation of extra-domain-specific FN variants to *Fn1 -/-* MFs. (**A**) Schematic representation of the expression of FN variants in assembly-incompetent HEK293 cells for purification from conditioned medium (CM). After purification, *Fn1 -/-* MFs are presented with the purified variants for functional analyses. (**B**) Western blot of whole cell lysates and conditioned medium of *Fn1 -/-* MFs presented with FN variants for 2 h. Quantification of FN bands in the conditioned medium verified the addition of equal amounts of FN to the cells, presented here as mean ±s.e.m. relative to the amount of FN B-A- (n = 9). Cell associated FN represents harvesting and deposition of FN variants by *Fn1 -/-* MFs shown as mean ±s.e.m relative to FN B-A-. ERK1/2 was used as loading control (n = 2 independent experiments performed at this

time point). (**C**) Immunofluorescence staining of FN and nuclei of *Fn1 -/-* MFs presented with FN variants for the indicated times (2 h, n = 2; 48 h, n = 3 independent experiments). Polymerized FN is located at areas of cell-cell contact (thick arrow) and retracting edges of polarized cells (thin arrow). The absence of FN polymerization can be noted at the leading edge of spread cells (arrowhead). In the 48-hour images, nuclei have been added as inserts. Scale bars: 50 µm.

Fig. 3. The effects of FN extra domains on cell growth and metabolism. (**A**) Growth curves of *Fn1 -/-* MFs stimulated with FN variants or vehicle buffer for 5 days (mean ±s.e.m.; n = 7). (**B**) Doubling time of cells treated with FN variants relative to cells treated with vehicle CTRL determined from the linear part of the exponential phase of growth (mean ±s.e.m.; n = 7). (**C**) Representative phase contrast images of *Fn1 -/-* MFs 5 days after stimulation with FN variants. Scale bar: 100 µm. (**D**) Medium acidification observed 4 days post treatment. (**E**) Extracellular acidification rate (ECAR) of *Fn1 -/-* MFs after a 72-hour treatment with FN variants or vehicle buffer measured with the Seahorse analyzer (mean ±s.d.; from 2 independent experiments; points represent the mean of technical triplicates). (**F**) Oxygen consumption rate (OCR) measured with the Seahorse analyzer in *Fn1 -/-* cells treated for 72 h with FN variants or vehicle buffer (mean ±s.d.; 3 technical repeats from 2 independent experiments). The color code is the same as in (A). (**G**) Intracellular pH measurements in cells treated with FN variants or vehicle CTRL after 48 h (n = 6). Results are represented as mean ±s.e.m ΔpH_i (difference in internal pH) relative to CTRL. (*$p \leq 0.05$; **$p \leq 0.01$; Student's *t* test).

Fig. 4. Regulation of TGF-β signaling by FN extra domain-containing variants. (**A**) Time course of TGF-b response gene expression. *Fn1 -/-* MFs were stimulated with FN variants for the indicated time points. Results are represented as mean ±s.e.m. fold change relative to vehicle control (CTRL) for each time point. Time points later than 8 h have been omitted for clarity (n = 4). (**B**) Time points at which changes in expression levels are the highest (2 h for *PAI1* and *CTGF*; 48 h for *TGFBI*). (**C**) Western blot displaying the phosphorylation of SMAD2 (p-SMAD2) after a 2-h stimulation of *Fn1 -/-* MFs with FN variants. Total SMAD2 used as loading CTRL. Numbers beneath the blots represent mean ±s.e.m. fold phosphorylation relative to CTRL (n = 3). (**D**) Western blot showing the decrease in SMAD2 phosphorylation following TGFBRI inhibition. *Fn1 -/-* MFs were treated with FN B+A+ and SB-431542, a TGFBRI inhibitor, and their respective vehicle solutions for control. Total SMAD2 was used as loading control. Numbers beneath the blots represent mean ±s.d. fold phosphorylation relative to respective CTRL (n = 2 independent experiments). (*$p \leq 0.05$; **$p \leq 0.01$; ***$p \leq 0.001$; Student's *t* test).

Fig. 5. The impact of the FN extra domains on FN assembly and ECM physical properties. (**A**) Variant-specific decellularized matrices. *Fn1 -/-* MFs were presented with FN variants for 7 days. Matrices were generated, decellularized, fixed and immunofluorescently stained for FN, type VI collagen, and TNC (n = 2 technical repeats from 2 independent experiments). Scale bar: 100 µm. (**B**) Matrix thickness measured with confocal microscopy (mean ±s.e.m.; n = 5). (**C**) FN variant-specific ECM stiffness was measured with atomic force microscopy (n = 3). Data from a representative experiment presented as box-and-whisker plots, with box borders representing the 25% and 75% of the interquartile range, and whiskers representing the 10% and 90% of the data points; median values are shown. $^{**}p \leq 0.01$; $^{***}p \leq 0.001$; $^{****}p \leq 0.0001$ (B, Student's t test; C, Kruskal-Wallis test for non-parametric distributions).

Fig. 6. Computational analyses of FN variant-specific matrices. (**A**) Matrices assembled by *Fn1 -/-* MFs presented with FN variants were decellularized after 7 days, stained for FN and visualized by confocal microscopy. Scale bar: 50 µm. (**B**) Confusion matrix of FN variant network classification using Convolutional Neural Networks. An algorithm was trained to recognize and classify FN-variant-specific matrices. The diagonal (in blue) displays the classification success rate (correctly classified images). (**C**) Flow chart of fiber analysis. **1**: confocal images were acquired and cropped to a final size of 512 × 512 pixels; **2**: a set of Gabor kernels representing an elemental-fiber dictionary was established; **3**: fiber detection was performed using Gabor kernels on acquired images; **4**: detected fibers were used to generate variant-specific morphological skeletons; **5**: feature extraction. (**D**) Graph-based representation of the FN variant fibers detected by Gabor kernels. Edges (black segments) connect nodes (red dots). (**E**) Principal component analysis (PCA) of the indicated features related to the graphs or derived from characteristic Gabor kernel parameters.

Figure 1

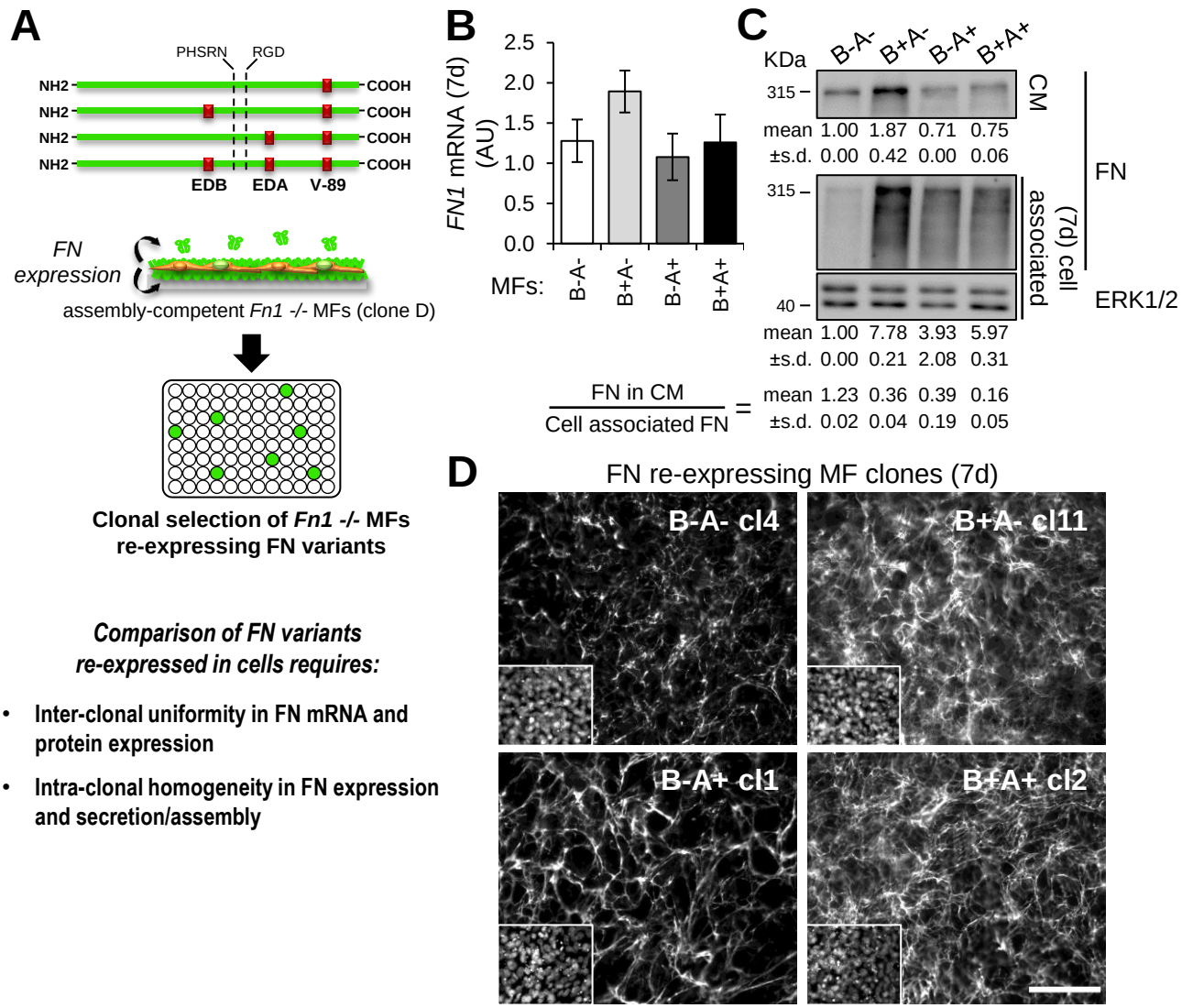

Comparison of FN variants re-expressed in cells requires:

- **Inter-clonal uniformity in FN mRNA and protein expression**
- **Intra-clonal homogeneity in FN expression and secretion/assembly**

Figure 2

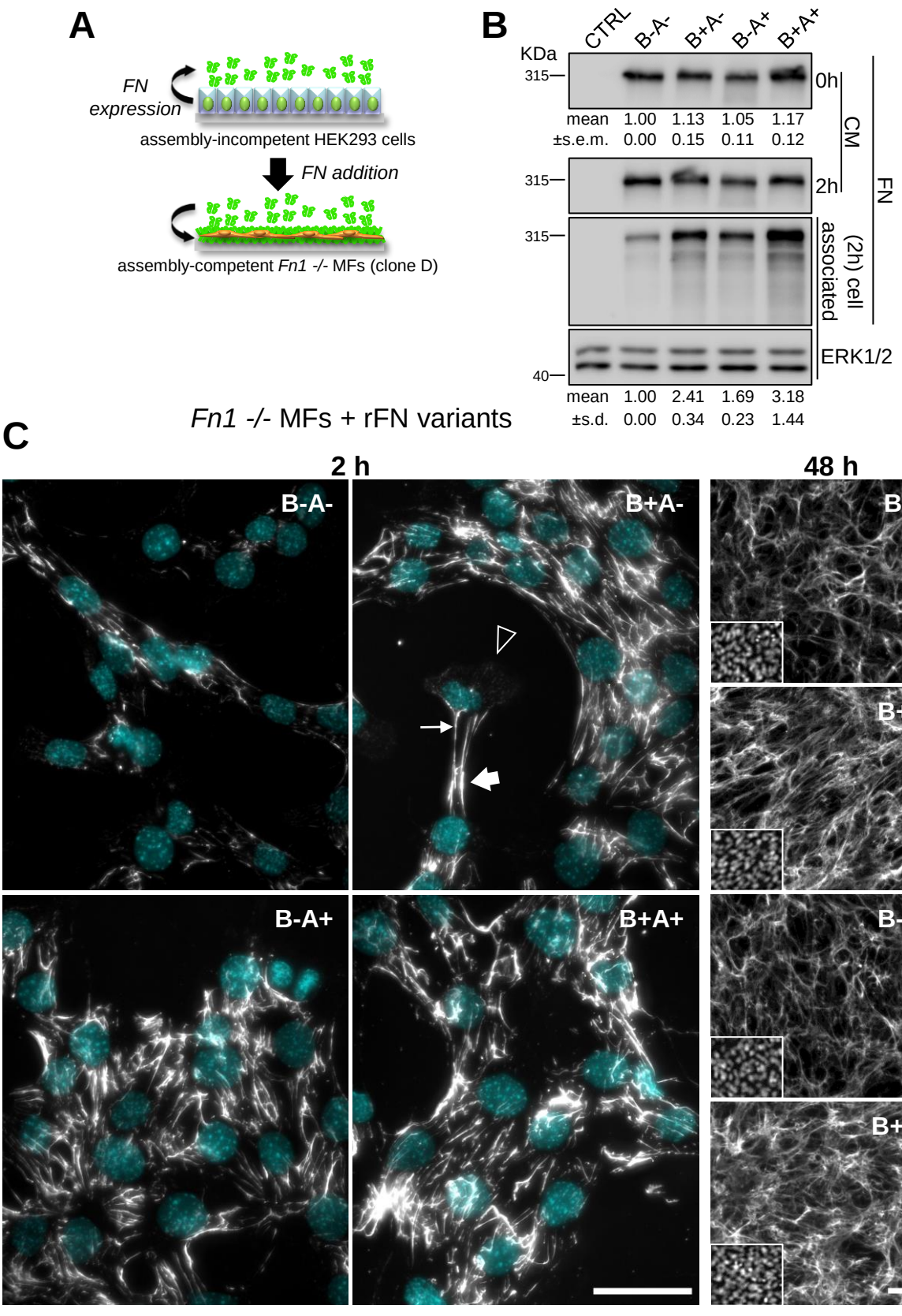
A
FN expression
assembly-incompetent HEK293 cells
FN addition
assembly-competent Fn1 -/- MFs (clone D)
B
CTRL
B-A-
B+A-
B-A+
B+A+
KDa
315
0h
mean 1.00 1.13 1.05 1.17
±s.e.m. 0.00 0.15 0.11 0.12
CM
315
2h
315
(2h) cell associated
FN
40
ERK1/2
mean 1.00 2.41 1.69 3.18
±s.d. 0.00 0.34 0.23 1.44
C
Fn1 -/- MFs + rFN variants
2 h
48 h
B-A-
B+A-
B-A+
B+A+

Figure 3

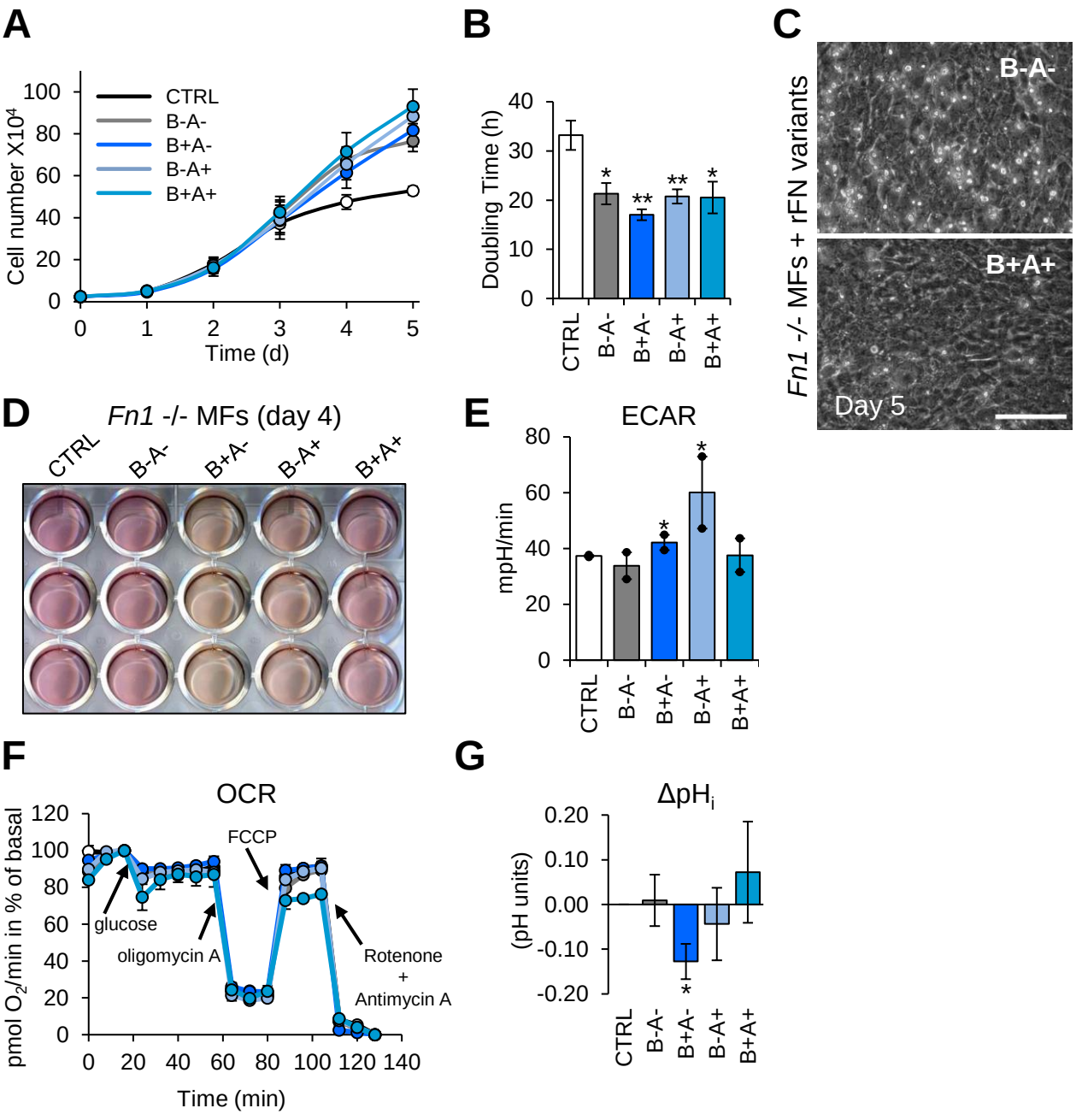
A
Cell number X10^4
Time (d)
CTRL
B-A-
B+A-
B-A+
B+A+
B
Doubling Time (h)
C
B-A-
B+A+
Fn1 -/- MFs + rFN variants
Day 5
D
Fn1 -/- MFs (day 4)
E
ECAR
mpH/min
F
OCR
pmol O2/min in % of basal
Time (min)
glucose
oligomycin A
FCCP
Rotenone
+
Antimycin A
G
ΔpHi
(pH units)

Figure 4

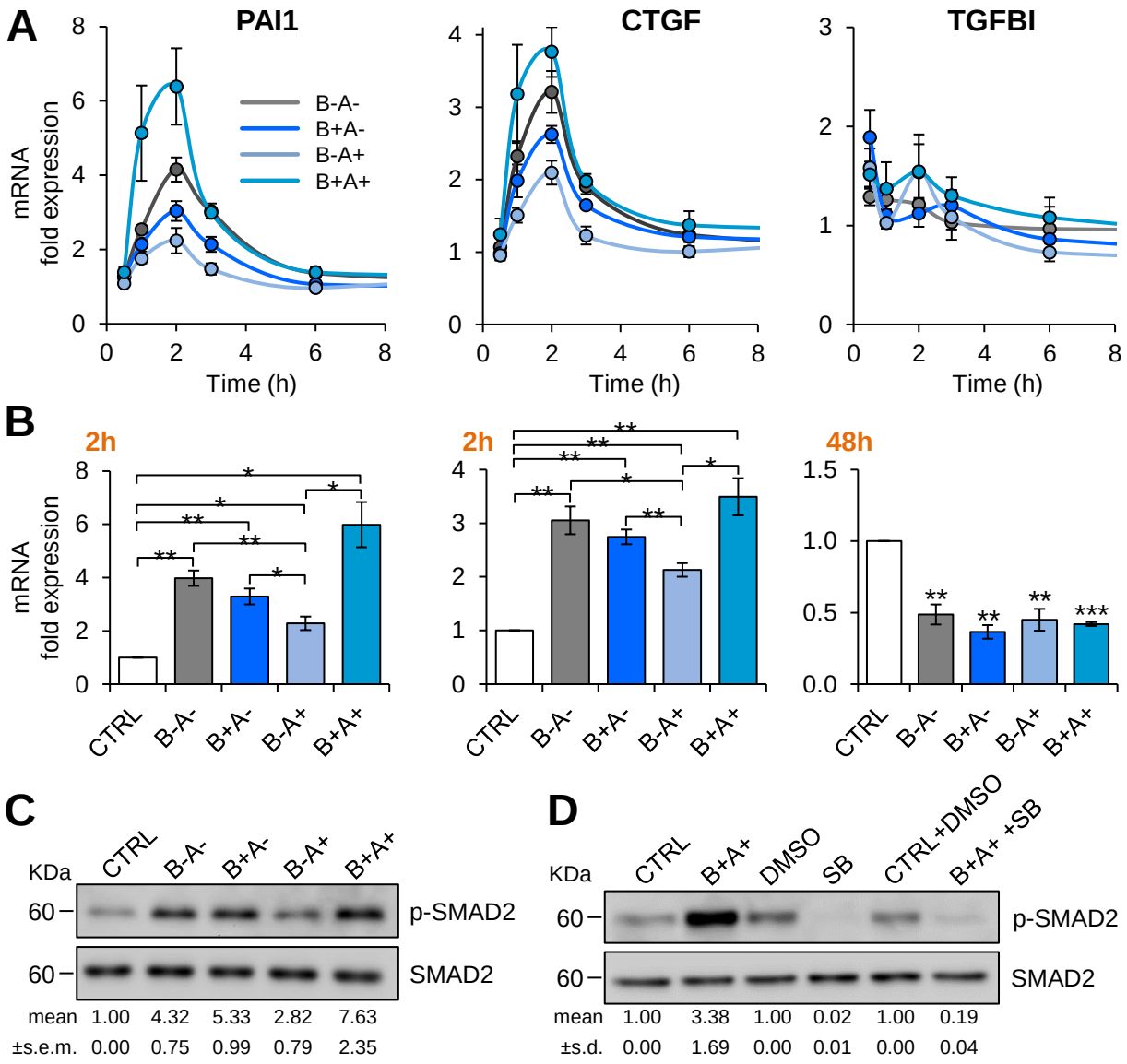
A
PAI1
CTGF
TGFBI
mRNA fold expression
Time (h)
B-A-
B+A-
B-A+
B+A+
B
2h
2h
48h
CTRL
B-A-
B+A-
B-A+
B+A+
C
KDa
p-SMAD2
SMAD2
mean 1.00 4.32 5.33 2.82 7.63
±s.e.m. 0.00 0.75 0.99 0.79 2.35
D
CTRL
B+A+
DMSO
SB
CTRL+DMSO
B+A+ +SB
p-SMAD2
SMAD2
mean 1.00 3.38 1.00 0.02 1.00 0.19
±s.d. 0.00 1.69 0.00 0.01 0.00 0.04

Figure 5

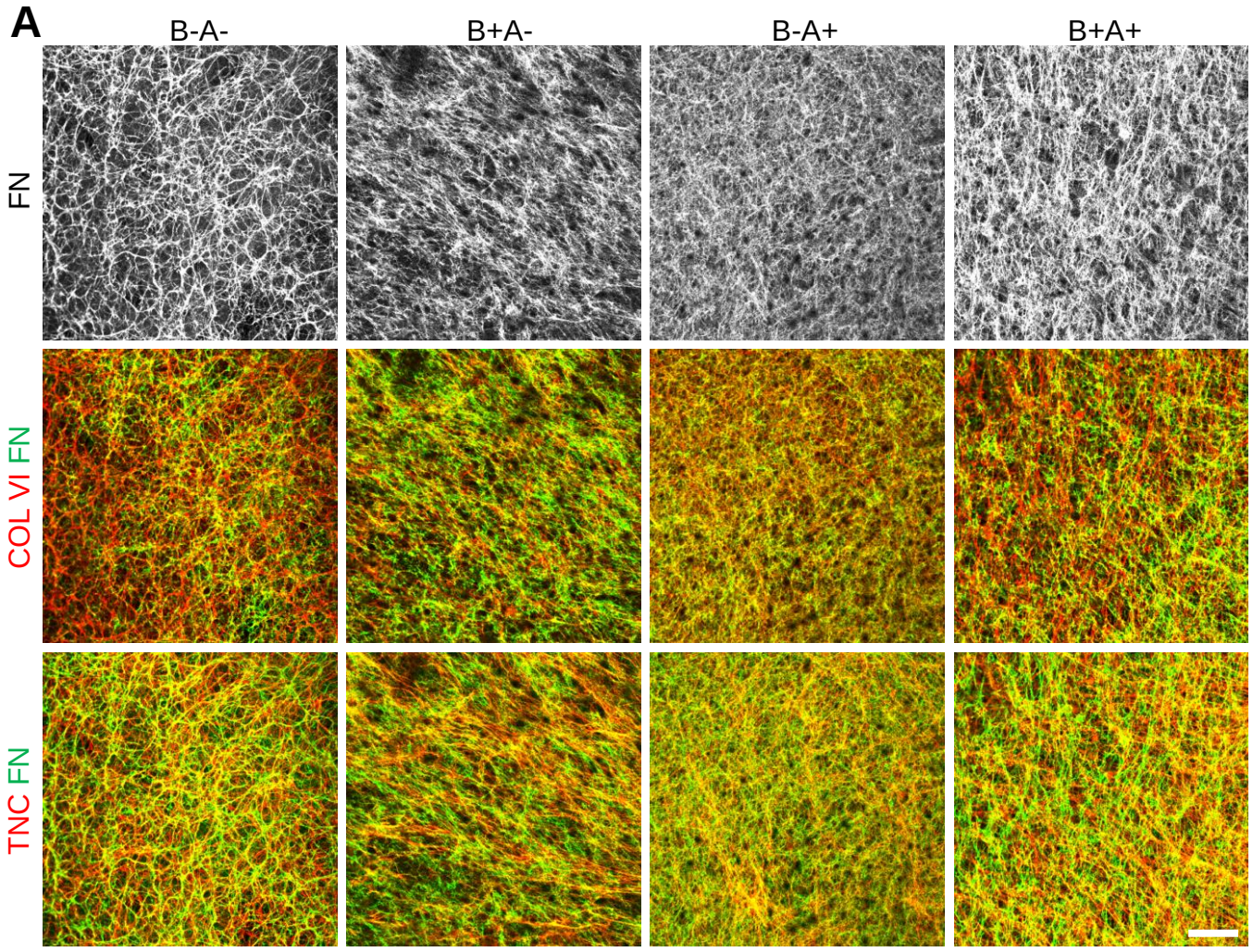
A
B-A-
B+A-
B-A+
B+A+
FN
COL VI FN
TNC FN

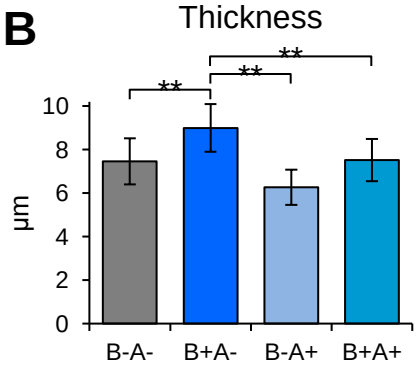
B
Thickness
µm
0
2
4
6
8
10
**
**
**
B-A-
B+A-
B-A+
B+A+

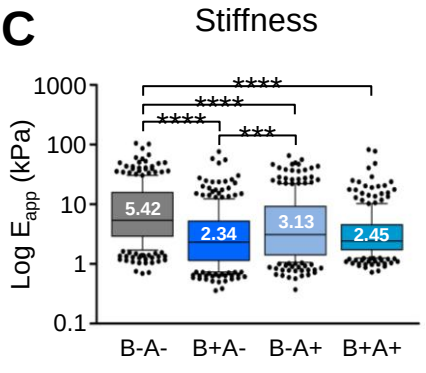
C
Stiffness
Log E_app (kPa)
0.1
1
10
100
1000
****
****
****
***
5.42
2.34
3.13
2.45
B-A-
B+A-
B-A+
B+A+

Figure 6

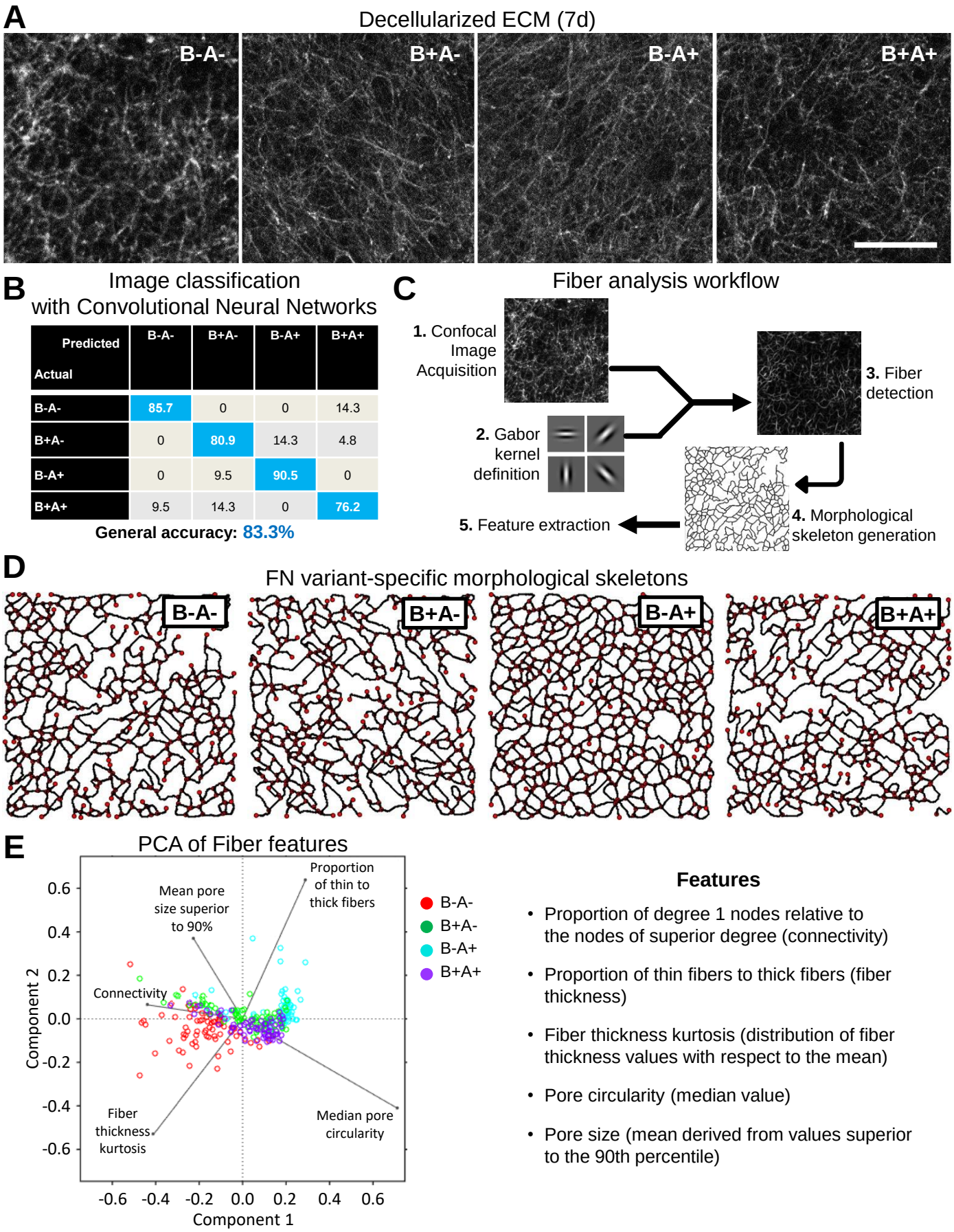
A
Decellularized ECM (7d)
B-A-
B+A-
B-A+
B+A+
B
Image classification
with Convolutional Neural Networks
Predicted
Actual
B-A-
B+A-
B-A+
B+A+
85.7
0
0
14.3
0
80.9
14.3
4.8
0
9.5
90.5
0
9.5
14.3
0
76.2
General accuracy: 83.3%
C
Fiber analysis workflow
1. Confocal Image Acquisition
2. Gabor kernel definition
3. Fiber detection
4. Morphological skeleton generation
5. Feature extraction
D
FN variant-specific morphological skeletons
B-A-
B+A-
B-A+
B+A+
E
PCA of Fiber features
Proportion of thin to thick fibers
Mean pore size superior to 90%
Connectivity
Fiber thickness kurtosis
Median pore circularity
Component 2
Component 1
0.6
0.4
0.2
0.0
-0.2
-0.4
-0.6
B-A-
B+A-
B-A+
B+A+
Features
• Proportion of degree 1 nodes relative to the nodes of superior degree (connectivity)
• Proportion of thin fibers to thick fibers (fiber thickness)
• Fiber thickness kurtosis (distribution of fiber thickness values with respect to the mean)
• Pore circularity (median value)
• Pore size (mean derived from values superior to the 90th percentile)

Supplementary Information

Supplementary Figures

Fig. S1. Generation of *Fn1 -/-* MF clones. (**A**) Relative amounts of FN mRNA containing EDB and/or EDA assessed by qRT-PCR (n = 4). (**B**) Schematic representation of the relevant position of the two LoxP sites flanking the first exon of the *Fn1* gene, and the positions of the primer set used to confirm the deletion. (**C**) Agarose gel electrophoresis of the PCR products generated from four separate *Fn1 fl/fl* populations infected with a lentiviral vector bearing the coding sequence of Cre recombinase. (**D**) Western analysis showing the elimination of FN protein in whole cell lysates and conditioned medium from *Fn1 -/-* MF Clone D. ERK was used as loading control (n = 4). (**E**) Phase contrast (top row) and immunofluorescent staining (middle and bottom rows) of FN displaying the absence of FN deposition in *Fn1 -/-* MF Clone D after 2 days in culture (n = 4). Scale bars: Phase, 200 µm; IF, 50 µm.

Fig. S2. Variability in FN variant expressing MFs. (**A**) Immunofluorescent staining of FN in the four selected clones. An anti-totalFN antibody was used in combination with an anti-EDB or anti-EDA to verify the expression of the FN variants by the different clones (B-A- cl4, B+A- cl11, B-A+ cl1, B+A+ cl2). Scale bar, 50 µm (n = 2). (**B**) FN mRNA and protein levels in three individual clones expressing FN B-A-. Numbers beneath the blot represent fold expression of FN relative to B-A- cl4 normalized to ERK. (**C**) FN mRNA and protein levels in three individual clones expressing FN B+A-. Numbers beneath the blot represent FN fold expression relative to B+A- cl11 normalized to ERK. (**D**) Immunofluorescent staining of three individual clones expressing FN B-A- [same as in (B)] and three individual clones expressing FN B+A- [same as in (C)] to compare FN expression and assembly across clones for 2 different FN variants after 7 days in culture. Nuclei are shown in the inserts. Scale bar: 50 µm (n = 2).

Fig. S3. Recombinant FN variant production in HEK293 cells. (**A**) Phase contrast (top row) and immunofluorescent staining of FN and nuclei (bottom row) of HEK293 cells stably expressing the FN variants or the empty vector. Scale bars: Phase, 50 µm; IF, 20 µm. FN is only observed in the cytoplasm and the plasma membrane before being secreted by the assembly-incompetent HEK293 cells. (**B**) Recombinant FN variant production by HEK293 cells determined by ELISA. (**C**) Silver staining of FN variants in polyacrylamide gels run under reducing and non-reducing conditions to verify the integrity of the proteins, as well as their ability to dimerize. (**D**) Western blot of FN variants run in polyacrylamide gels and stained with different antibodies against total FN, Extra Domain B, and Extra Domain A verifying the all-or-nothing inclusion of the Extra Domains in each variant. (**E**) Immunofluorescent staining of FN-coated (3

μg/ml) glass coverslips to assess the existence of aggregates, that would greatly affect solubility and bioavailability. Arrowheads indicate examples of isolated FN aggregates. Scale bar: 50 μm. (**F**) Immunofluorescent staining of FN (left column) and phase contrast (right column) of *Fn1 -/-* MFs 5 days after having been presented with increasing concentrations of pFN to find the optimal concentration for our studies. We determined that 15 μg/ml is a good compromise between efficient matrix generation and moderation in the use of the purified variants.

Fig. S4. Integrin α5 and β3 distribution in MFs treated with FN variants. Immunofluorescent staining of FN assembly and integrin α5 and β3 localization in MFs stimulated with recombinant FN variants for 2 h. Scale bar, 50 μm. Thin arrows show the FN polymerization along the rear edge of polarized cells. Thick arrows indicate sites of readily polymerized cFN at areas of cell-cell contact. Arrowheads point the absence of FN polymerization at the leading edge of spread cells where αvβ3 focal adhesions are more prominent (n = 2).

Fig. S5. Metabolic effects of FN variants in *Fn1 -/-* MFs and TGF-β detection in FN preparations and conditioned media of *Fn1 -/-* MFs. (**A**) Glucose uptake in *Fn1 -/-* MFs stimulated with FN variants for 48 h. Results are displayed as mean ±s.e.m. fold uptake relative to CTRL (n = 9). (**B**) Extrusion of lactate in the culture medium of *Fn1 -/-* MFs treated with FN variants for 48 h, represented as mean ±s.e.m. fold difference relative to day 0 CTRL (n = 2). (**C**) and (**D**) Expression of mRNA encoding glyceraldehyde phosphate dehydrogenase (GAPDH) mRNA and phosphoglycerate kinase 1 (PGK1), enzymes that catalyze the 6th and 7th steps of glycolysis respectively, was determined in *Fn1 -/-* MFs after 48 h of stimulation with FN variants (n = 4). (**E**) Extracellular acidification rate in response to glucose measured in *Fn1 -/-* MFs stimulated for 72 h with FN variants with the Seahorse analyzer. (**F**) Basal mitochondrial activity of *Fn1 -/-* MFs stimulated with FN variants for 72 h, determined with the Seahorse analyzer by measuring oxygen consumption rate (OCR). (**G**) Maximal mitochondrial activity of *Fn1 -/-* MFs stimulated with FN variants for 72 h, measured as in (E). (**H**) *Fn1 -/-* MFs were stimulated with FN variants for 72 h and OCR was determined in response to glucose with the Seahorse analyzer. (**I**) Dependence of respiration of *Fn1 -/-* MFs stimulated with FN variants on ATP synthase demonstrated with the Seahorse analyzer (n = 2). (**J**) TGF-β1 detection in recombinant FN preparations. FN preparations were added in DMEM (15 μg/ml) to assess the presence of TGF-β1. Standard culture medium (DMEM +5% FCS) was used as reference. (**K**) Total TGF-β1 concentration in the conditioned medium of *Fn1 -/-* MFs stimulated with 15 μg/ml of recombinant FN variants for 2 h (n = 2). (**L**) Collagen based gel contraction assay. *Fn1 -/-* MFs were

embedded in collagen lattices containing FN variants. Cell surface reduction was measured after a 24-hour incubation following lattice solidification (n = 4).

Fig. S6. Feature distribution across FN variant matrices. (**A**) Connectivity graph displaying the ratio of degree-1 nodes relative to higher-degree nodes. (**B**) Thickness graph showing the distribution of thin fibers relative to thick fibers as described in materials and methods. (**C**) Graph representing the heterogeneity in fiber thickness across the different matrices, as determined by the fiber thickness kurtosis distribution. (**D**) Median pore circularity distribution defined by pore area and perimeter. (**E**) Average pore size distribution across FN matrices after filtering out pores below the 90th percentile within each distribution.

Supplementary Tables

Table S1. Primary antibodies list used, suppliers and dilutions.

Specificity	Company	Clone	Reference	Raised in	Application
anti-FN-EDA	Sirius Biotech	IST-9	S-FN5	Mouse	WB: 1/200 IF: 1/200
anti-FN-EDB	Sirius Biotech	C6	S-FN12	Mouse	WB: 1/200 IF: 1/200
anti-FN	Millipore	Polyclonal	AB1945	Rabbit	WB: 1/1000 IF: 1/400
anti-FN	BD Biosciences	10/Fibronectin	#610077	Mouse	WB: 1/1000 IF: 1/500
anti-ERK1/2 (diphosphorylated)	Sigma-Aldrich	MAPK-YT	M8159	Mouse	WB: 1/1000
anti-ERK1/2	Santa Cruz Biotechnology	C-16	sc-93	Rabbit	WB: 1/2000
anti-SMAD2 (Ser465/467)	Cell Signaling Technology	138D4	#3108	Rabbit	WB: 1/1000
anti-SMAD2	Cell Signaling Technology	86F7	#3122	Rabbit	WB: 1/2000
anti-α5	Chemicon	Polyclonal	AB1928	Rabbit	IF: 1/1000
anti-β3	Emfret	Luc.A5	M030-0	Rat	IF: 1/500
anti-COL VI	Millipore	VI-26	MAB3303	Mouse	IF: 1/200
anti-TNC	Sigma-Aldrich	BC-24	T2551	Mouse	IF: 1/200

Table S2. Primers sequences used for qPCR studies.

Primer Name	Sequence	
	Forward	Reverse
mTbp	GAA-GAA-CAA-TCC-AGA-CTA-GCA-GCA	CCT-TAT-AGG-GAA-CTT-CAC-ATC-ACA-G

h1_FN_2K7	CCC-AAT-TGA-GTG-CTT-CAT-GCC	TGT-ACA-AGA-AAG-CTG-GGT-CG
mFn1	CTG-TAG-CAC-AAC-TTC-CAA-TTA-CGA-A	GGA-ATT-TCC-GCC-TCG-AGT-CT
mFN-EDB	TGG-TCC-ATG-CTG-ATC-AGA-GT	CCT-CAG-GCC-GAT-GCT-TGA-AT
mFN-EDA	GGA-GCT-TTT-CCC-TGC-ACC-TG	GTG-GGT-GTC-ACC-TGA-CTG-AA
mTgfbi	AAG-GTC-ATT-GGC-ACC-AAC-AAG	AAC-CTT-TCT-CTC-CTG-GGA-CCT-T
mCtgf	CAG-CTG-GGA-GAA-CTG-TGT-ACG	GTA-CAC-CGA-CCC-ACC-GAA-GA
mPai1	TGA-GCT-GTG-CCC-TTC-TCA-TT	GCC-ACC-GAC-TTC-GGA-GTA-AA
Mycoplasma sp.	GGG-AGC-AAA-CAG-GAT-TAG-ATA-CCC-T	TGC-ACC-ATC-TGT-CAC-TCT-GTT-AAC-CTC

73

74

Supplementary Figure 1

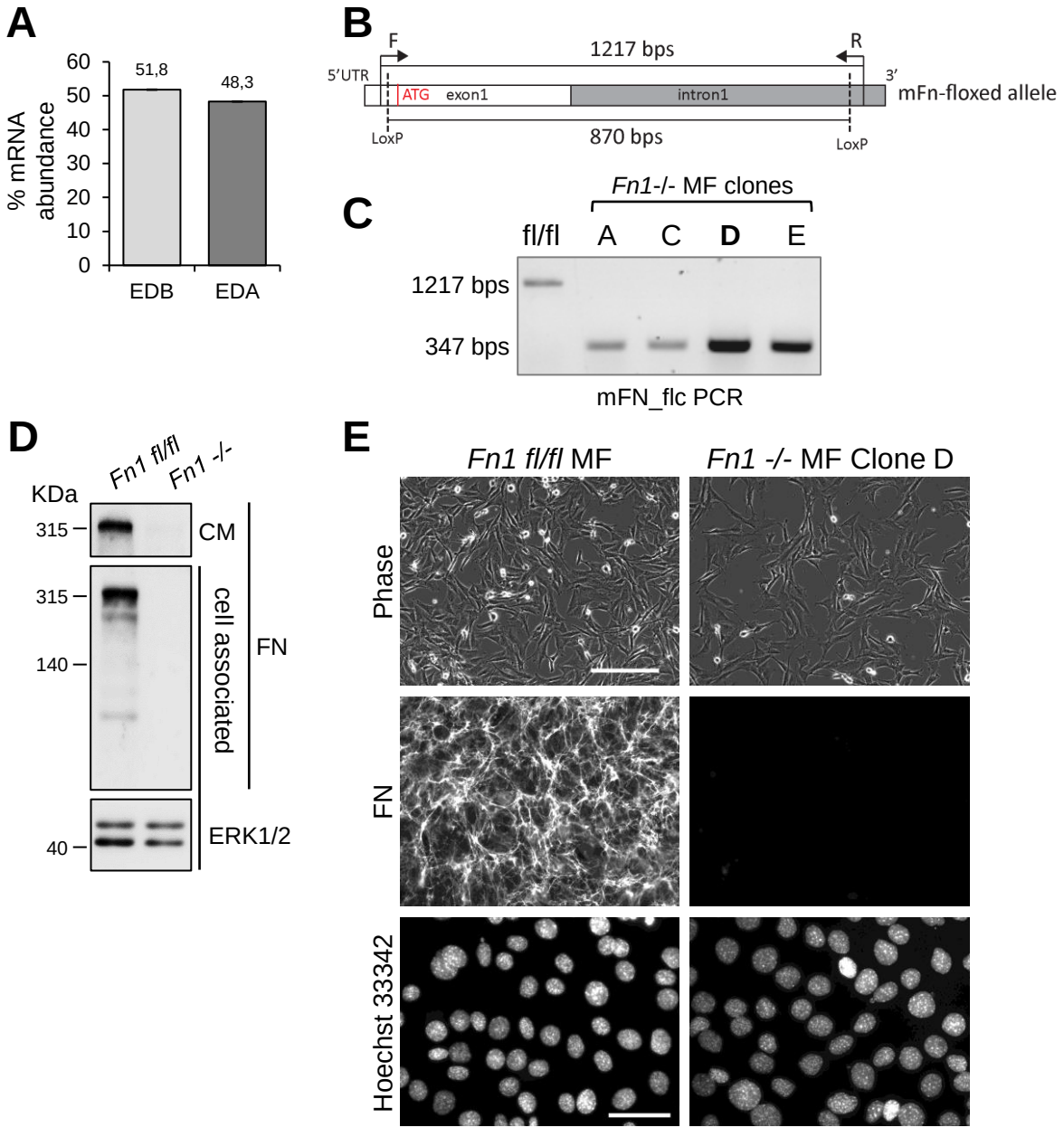

Supplementary Figure 2

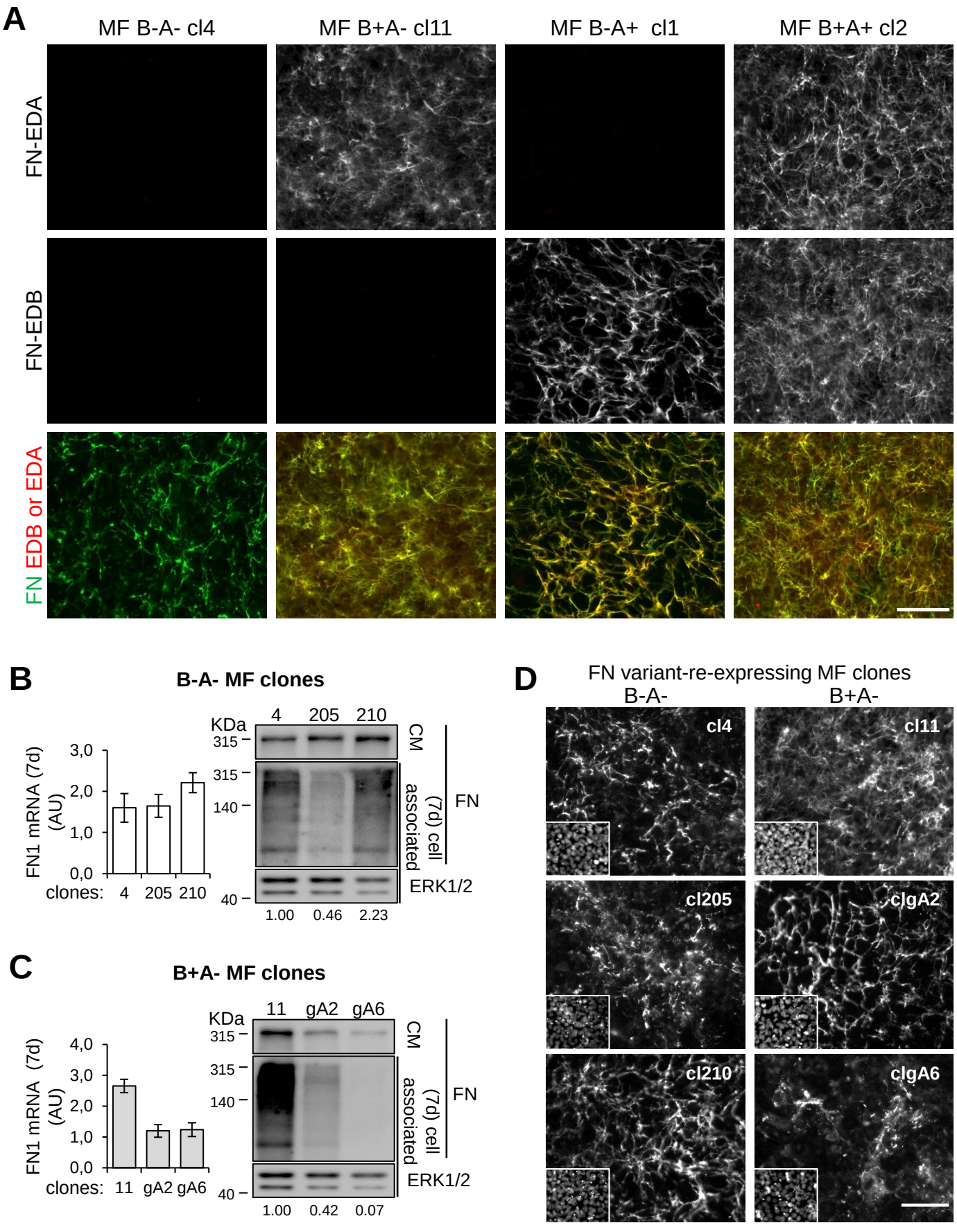

Supplementary Figure 3

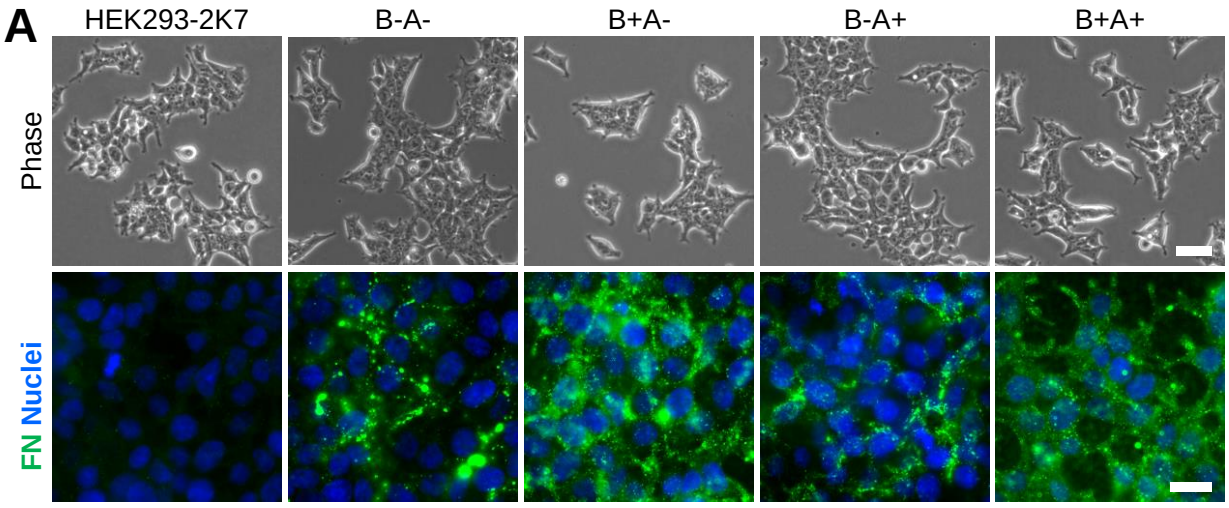

B Elisa

	FN1 (µg/ml)
HEK293	0.53
vector cl4	0.33
B-A- cl16	13.5
B+A- cl4	6.83
B-A+ cl4	30.2
B+A+ cl25	16.7

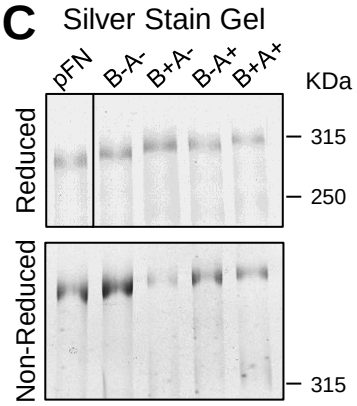

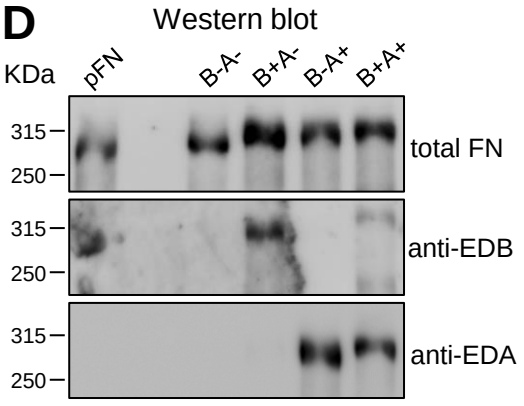

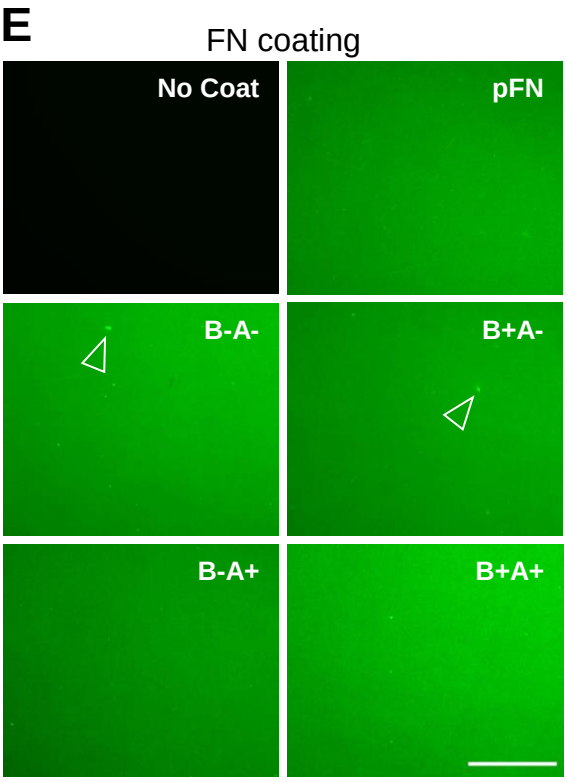

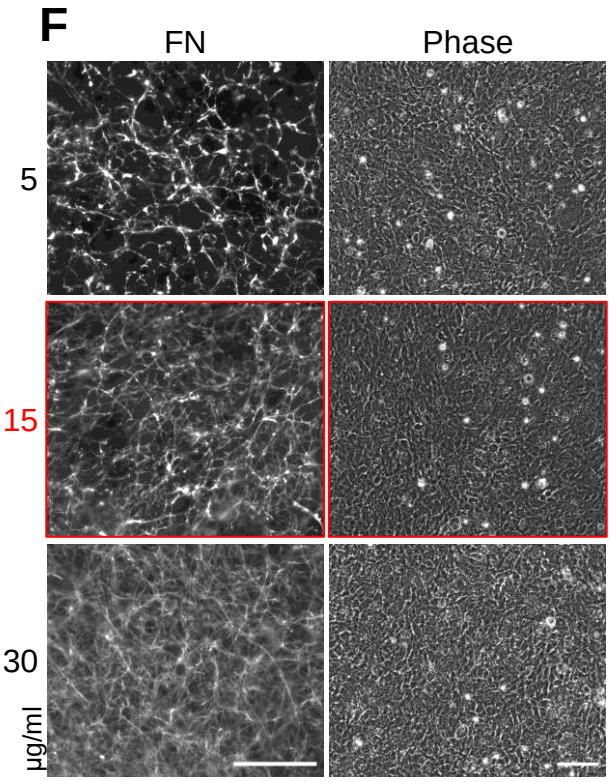

Supplementary Figure 4

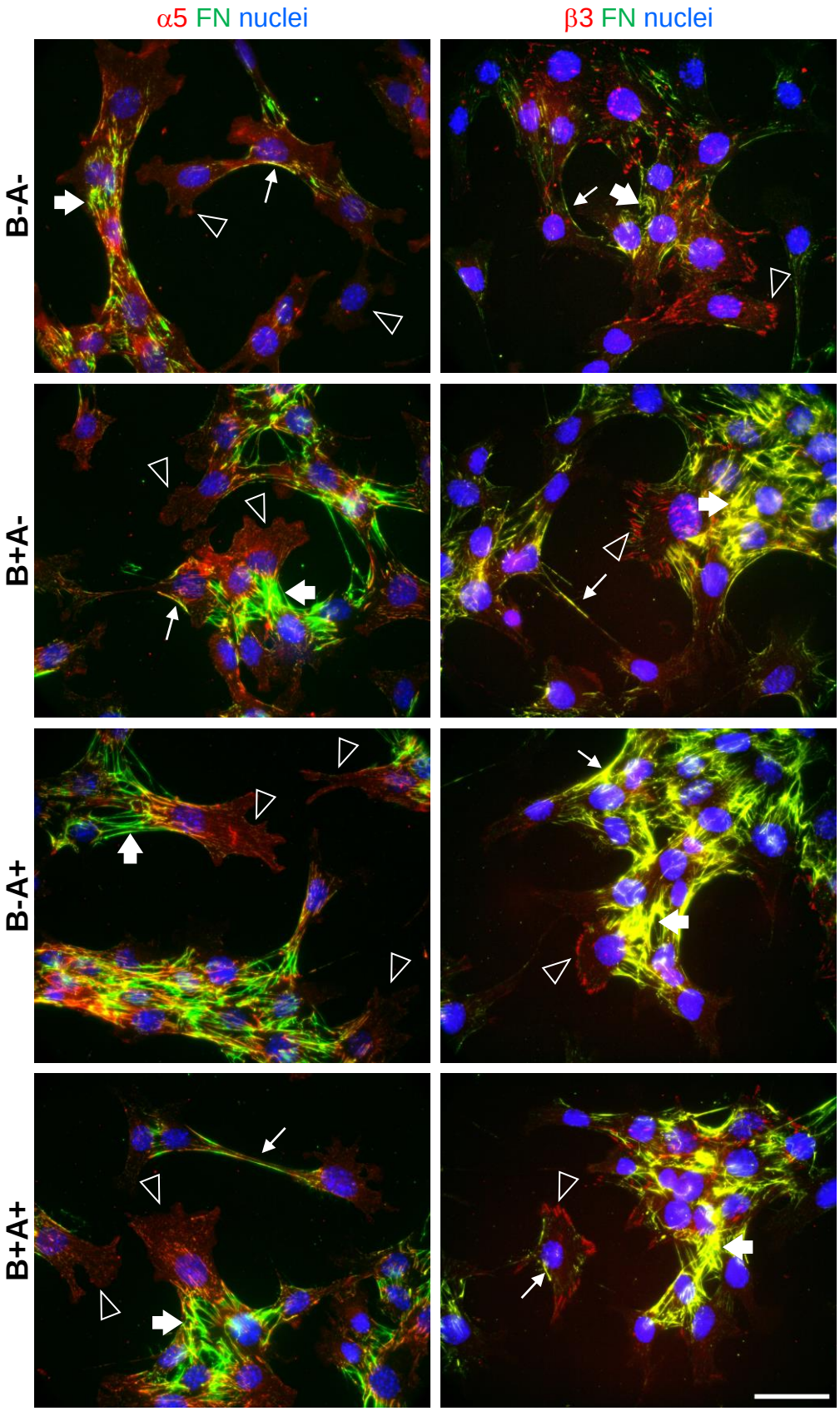

Supplementary Figure 5

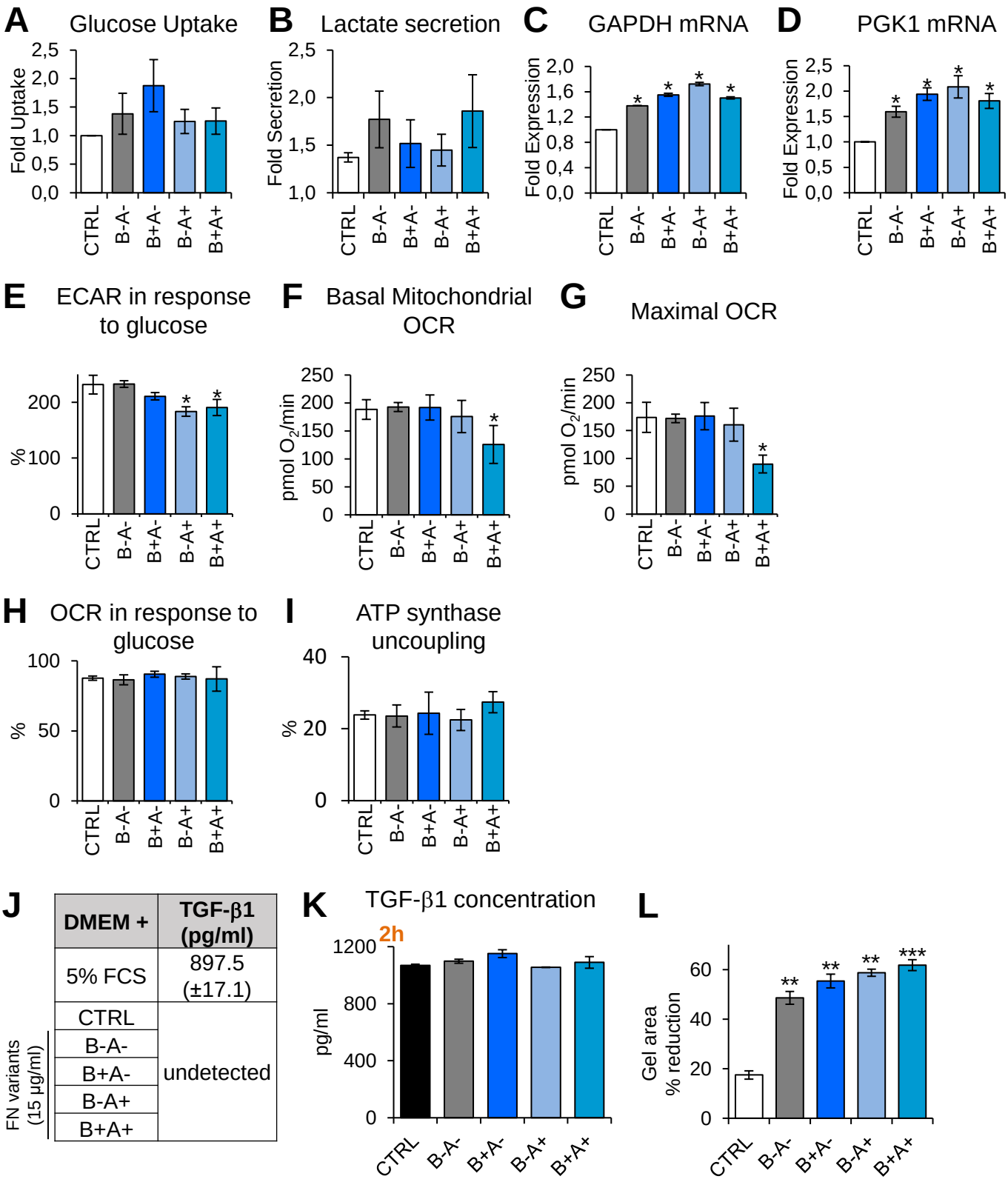

J

DMEM +	TGF-β1 (pg/ml)
5% FCS	897.5 (±17.1)
CTRL	undetected
B-A-	
B+A-	
B-A+	
B+A+	

FN variants (15 µg/ml)

Supplementary Figure 6